Evaluation of scale-resolving simulations for a turbulent channel flow

Klapwijk, M.; Lloyd, T.; Vaz, G.; van Terwisga, T.

DOI
10.1016/j.compfluid.2020.104636

Publication date
2020

Document Version
Final published version

Published in
Computers and Fluids

Computers and Fluids 209 (2020) 104636

Contents lists available at ScienceDirect

Computers and Fluids

journal homepage: www.elsevier.com/locate/compfluid

Evaluation of scale-resolving simulations for a turbulent channel flow

M. Klapwijk [a,b,*], T. Lloyd [b], G. Vaz [b,c], T. van Terwisga [a,b]

[a] Delft University of Technology, Mekelweg 2, 2628 CD, Delft, The Netherlands
[b] Maritime Research Institute Netherlands, Haagsteeg 2, 6708 PM, Wageningen, The Netherlands
[c] WavEC - Offshore Renewables, Edifício Diogo Cão, Doca de Alcântara Norte, Lisbon, 1350-352, Portugal

ARTICLE INFO

Article history:
Received 24 July 2019
Revised 19 March 2020
Accepted 19 June 2020
Available online 20 June 2020

Keywords:
Turbulent channel flow
Verification
DES
LES
PANS
Synthetic turbulence

ABSTRACT

Different variable resolution turbulence modelling approaches (Hybrid, Bridging models and LES) are evaluated for turbulent channel flow at $Re_\tau = 395$, for cases using either streamwise periodic boundary conditions or a synthetic turbulence generator. The effect of iterative, statistical and discretisation errors is investigated. For LES, little difference between the different sub-filter modelling approaches is found on the finer grids, while on coarser grids ILES deviates from explicit LES approaches. The results for Hybrid models are strongly dependent on their formulation, and the corresponding blending between the RANS and LES regions. The application of PANS with different ratios of modelled-to-total kinetic energy, f_k, shows that there is no smooth transition in the results between RANS and DNS. Instead a case-dependent threshold which separates two solution regimes is observed: f_k values below 0.2 yield a proper turbulent solution, similar to LES results; higher f_k values lead to a laminar flow due to filtering of the smallest scales in the inverse energy cascade. The application of a synthetic turbulence generator is observed to yield similar performance for all models. The reduced computational cost and increased flexibility makes it a suitable approach to enable the usage of SRS for industrial flow cases which depend on the development of a turbulent boundary layer. It ensures that sufficient large-scale structures develop over the full boundary layer height, thereby negating the problem of relying on the inverse energy cascade for the development of turbulence. Both LES and PANS with turbulence generator yield a better match with the reference data than Hybrid models; of these methods PANS is preferable due to the separation of modelling and discretisation errors.

1. Introduction

The application of Computational Fluid Dynamics (CFD) in the maritime sector is moving towards more complex problems, such as massively separated flows, blunt bodies, off-design conditions, cavitation and noise predictions. For such cases the assumptions in traditional unsteady Reynolds Averaged Navier-Stokes (RANS) approaches are too limiting, leading to an underprediction or absence of correct unsteady flow phenomena. Resolving the full spectrum of turbulence by means of Direct Numerical Simulation (DNS) remains out of reach due to excessive computational cost, leading to a focus on Scale-Resolving Simulations (SRS), where the larger scales are resolved, with the smaller scales modelled. The increase in available computational power makes this possible for high Reynolds number flows. In SRS, the added physical resolution should lead to a more accurate description of the flow and a reduction of the modelling error at a more reasonable cost. The decrease in modelling error leads to an increase in importance of numerical errors, thereby making error analysis even more relevant.

SRS can be divided into three main categories: Large Eddy Simulation (LES), for which an (implicit or explicit) filter is applied throughout the computational domain, resulting in scales larger than the filter being resolved and smaller scales being modelled using a 'sub-filter' model. The need to resolve a substantial part of the turbulence spectrum leads to stringent grid requirements in near wall regions, and therefore often to excessive computational cost for industrial flow problems, which typically involve complex geometries and Reynolds numbers which often exceed 10^6 in hydrodynamic applications [1]. The cost can be reduced through the use of wall modelled LES (WMLES), although the definition of the interface between wall model and resolved flow is difficult for complex geometries. This has lead to the rise of two alternative approaches: 'Hybrid' methods, where LES is zonally combined with

* Corresponding author.
E-mail address: m.d.klapwijk@tudelft.nl (M. Klapwijk).

https://doi.org/10.1016/j.compfluid.2020.104636

RANS, which is applied in regions where the grid cannot support LES resolution; and 'Bridging' methods, such as Partially Averaged Navier-Stokes (PANS) [2]. Bridging methods consist of a blending of RANS and DNS, but, in contrast to Hybrid methods, the blending is not location dependent. Instead it depends on user-defined settings, thereby allowing a smooth transition between the turbulence modelling approaches. This prevents commutation errors in the transition between RANS and LES zones, as occurs for Hybrid methods [3–5]. In the case of the PANS model the blend depends on the modelled-to-total ratios of turbulence kinetic energy, f_k, and dissipation, f_ϵ.

In all approaches the ratio between resolved and modelled turbulence depends on a filter length. In LES and Hybrid models this filter length is implicitly defined by the grid, i.e. refining the grid reduces the influence of the sub-filter model. Non-zonal Hybrid models have the additional issue that the blending function between LES and RANS depends on the local grid density. Consequently, with grid refinement not only the effect of the LES sub-filter model reduces in the LES region, but also a larger region of the flow is solved using LES. The modelling error is therefore entangled with, and for ILES even dependent on, the discretisation error, leading to a large grid sensitivity. These properties make estimating the discretisation error impossible, and grid refinement studies to verify the results difficult. Both of these are essential to enable Verification and Validation processes which are needed to assess the credibility of industrial CFD calculations. An advantage of Bridging models is that the filter length is set explicitly, thereby theoretically decoupling the discretisation and modelling errors. Of course, when performing a computation with a high physical resolution on a coarse grid, the discretisation error will become dominant. Due to these properties, Bridging models are becoming attractive for industrial CFD, where extensive grid refinement studies are often unaffordable while an estimate of the numerical error is still required [6,7].

Linked to the increased physics in SRS is the requirement of more physical inflow boundary conditions. It has been repeatedly shown that the results of LES or DNS can be dependent on inflow conditions, e.g. [8,9]. For SRS of turbulent flows which do not exhibit strong separated vortical structures, it is necessary that the inflow contains time-varying stochastic fluctuations which resemble turbulence. If this is not addressed, laminar solutions can be obtained, and consequently integral quantities, such as mean forces, can be underpredicted [10]. For attached, weakly unsteady flows, unphysical laminar separation may occur easily since transition to turbulence is significantly delayed. Ironically, this implies that for computing mean forces RANS methods often yield the best results for such flows. Hybrid methods also better predict mean forces, due to the use of RANS inside the boundary layer, resulting for example in superior prediction of velocity gradients close to the wall, when using steady inflow. However, at the interface between RANS and LES regions not all the modelled turbulence is transferred directly into resolved turbulence, leading to an overly laminar flow field. In such cases, inflow turbulence might still be necessary. While this problem has been known for a number of years, many publications using SRS still do not apply a proper inflow. These works often focus on turbulent structures and dynamics which appear satisfactory, yet the forces simultaneously show a large mismatch with experimental data. This discrepancy in integral quantities leads to difficulties in the validation of numerical results, and deteriorates the credibility of SRS for practical applications. Currently, the need for synthetic turbulence generation hampers the usage of SRS for industrial cases, such as cavitation and noise research for ship propellers.

Inflow turbulence can be generated either by precursor methods (such as a channel flow), or by synthetic methods, which do not rely on flow recycling. Precursor methods are generally noted for their accuracy, although they are more expensive to use due to the need to generate turbulence in a second, separate, domain. Their use is also often limited to canonical flows. Synthetic methods are cheaper to use, easier to tune to a desired set of turbulent inflow statistics, and more generally applicable [11]. These properties make a synthetic method preferable for industrial CFD, despite the requirement of a development length to allow the introduced fluctuations into develop to 'real' turbulence. In the case of cavitation and noise prediction, a further requirement is that the inflow velocity fluctuations are divergence-free, thereby avoiding spurious pressure fluctuations which can pollute the entire domain for incompressible computations.

It is well known that the choice of SRS model affects the flow prediction around the object of interest, although a subject less well addressed in the literature is the model interaction with the propagation of inflow turbulence. Consequently, an evaluation of different SRS methods in combination with inflow turbulence is necessary. This paper attempts to provide a systematic overview of the effect of SRS turbulence modelling approaches, both with streamwise periodic boundary conditions and with a synthetic turbulence generator. Full comparisons between different SRS approaches, including higher order moments, are rare in literature [12]; often, different codes, grids and solver settings are used, which makes it difficult to assess the modelling error of the turbulence modelling approaches. Models included in this paper are Hybrid (DDES [13], IDDES [14]) and XLES [15]); Bridging (PANS [2] with $f_k \in [0.05,\ 1.00]$); and LES (Smagorinsky [16], Lilly [17,18], WALE [19], KSGS [20] and ILES). Attention is paid to the assessment of iterative, discretisation and statistical errors.

The chosen test case is a turbulent channel flow at $Re_\tau = 395$, a canonical test case for the study of wall-bounded turbulence, due to the simple geometry and abundance of reference data. Experimental results are first published ninety years ago, and numerical studies have been performed using LES and DNS since the 1980s. Fig. 1 shows an overview of numerical results available in the open literature. It is observed that a range in total number of grid cells is applied for LES/DNS approaches at lower Re_τ values. DES and PANS results have been published for significantly higher Re_τ, but often without refining the grid. Most results shown are obtained using a finite volume approach, with second-order accurate discretisation schemes. Fig. 1 also shows an overview of the usage of synthetic turbulence generation methods available in the open literature, sorted per test case.

In the paper, Section 2 describes the different turbulence approaches used, and Section 3 describes the test case, numerical setup and turbulence-generating method. After an assessment of the numerical errors in Section 4, Sections 5 and 6 compare the results for Hybrid, Bridging and LES approaches using streamwise periodic boundary conditions and a synthetic turbulence generator respectively. Finally, Section 7 discusses the implications of the results for industrial test cases, followed by the conclusions in Section 8.

2. Mathematical turbulence approaches

In this work different approaches for modelling turbulence are applied, including Hybrid and Bridging models and LES. The main equations of these approaches are described in this section, with full model details given in Appendix A.

For all approaches considered the instantaneous quantities, Φ, can be decomposed into a resolved, $\langle\Phi\rangle$, and a modelled (unresolved) component, ϕ, according to $\Phi = \langle\Phi\rangle + \phi$ [46]. Applying this decomposition to the incompressible, single-phase, Newtonian Navier-Stokes equations leads to

$$\frac{\partial \langle U_i \rangle}{\partial x_i} = 0, \tag{1}$$

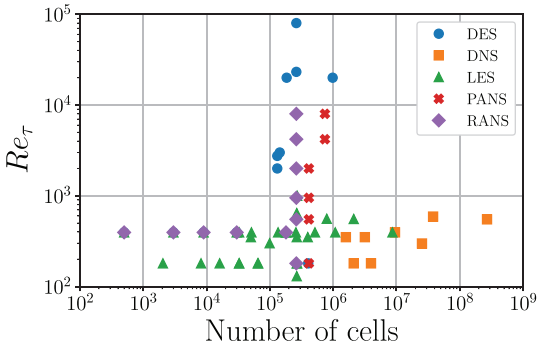

Test case	DFM	FSM	FM	SEM
Decaying homogeneous	1	1	2	2
Channel flow	5	1		4
Airfoil	1		1	
Airfoil trailing edge				1
Square duct				1
Plane jet	1			
Staggered cube array	1			

Fig. 1. Literature overview with a selection of the available numerical results. Turbulent channel flow results (left) as function of the number of grid cells, N_c, and the turbulence modelling approach (left) [21–35]. Usage of synthetic turbulence generation (right) sorted by test case and method (Digital Filtering (DFM), Forward Stepwise (FSM), Fourier (FM) and Synthetic Eddy method (SEM) [8,9,36–45].

$$\frac{\partial \langle U_i \rangle}{\partial t} + \langle U_j \rangle \frac{\partial \langle U_i \rangle}{\partial x_j} = -\frac{1}{\rho}\frac{\partial \langle P \rangle}{\partial x_i} + \frac{\partial}{\partial x_j}\left[\nu\left(\frac{\partial \langle U_i \rangle}{\partial x_j} + \frac{\partial \langle U_j \rangle}{\partial x_i}\right)\right] + \frac{1}{\rho}\frac{\partial \tau(u_i, u_j)}{\partial x_j}. \tag{2}$$

In these equations U_i denotes the velocity components, P the pressure, ν the kinematic viscosity, ρ the density and $\tau(u_i, u_j)$ the sub-filter stress tensor which is modelled using Boussinesq's hypothesis,

$$\tau(u_i, u_j) = \langle U_i U_j \rangle - \langle U_i \rangle \langle U_j \rangle = 2\nu_t \langle S_{ij} \rangle - \frac{2}{3} k \delta_{ij}, \tag{3}$$

with ν_t the eddy-viscosity, k the modelled turbulence kinetic energy, δ_{ij} the Kronecker delta and $\langle S_{ij} \rangle$ the resolved strain-rate tensor, defined as

$$\langle S_{ij} \rangle = \frac{1}{2}\left(\frac{\partial \langle U_i \rangle}{\partial x_j} + \frac{\partial \langle U_j \rangle}{\partial x_i}\right). \tag{4}$$

The difference between the respective approaches lies in the definition of the filtering operator $\langle \cdot \rangle$, which is temporal in the case of RANS and spatial for LES and PANS. Consequently, the sub-filter stress tensor is modelled differently by employing different expressions for ν_t and k.

2.1. RANS

In unsteady RANS, all turbulent time scales and motions are modelled, and a scale separation between deterministic and stochastic scales is assumed. In this work, the sub-filter stress tensor is modelled using the $k-\omega$ Shear Stress Transport (SST) model (2003 version) [47]. This model forms the basis of the Hybrid and Bridging models. It is a blend of a $k-\omega$ model in the wall region and a $k-\epsilon$ model in the far field. The transport equations are

$$\frac{\mathrm{D}k}{\mathrm{D}t} = P_k - \beta^* \omega k + \frac{\partial}{\partial x_j}\left((\nu + \nu_t \sigma_k)\frac{\partial k}{\partial x_j}\right), \tag{5}$$

$$\frac{\mathrm{D}\omega}{\mathrm{D}t} = \frac{\alpha}{\nu_t} P_k - \beta \omega^2 + \frac{\partial}{\partial x_j}\left[(\nu + \nu_t \sigma_\omega)\frac{\partial \omega}{\partial x_j}\right] + 2(1 - F_1)\frac{\sigma_{\omega_2}}{\omega}\frac{\partial k}{\partial x_j}\frac{\partial \omega}{\partial x_j}. \tag{6}$$

The other relevant expressions are

$$P_k = \min\left(\nu_t \langle |S| \rangle, 10\beta^* k\omega\right) \quad \text{and} \quad \nu_t = \frac{a_1 k}{\max\left(a_1 \omega, \langle |S| \rangle F_2\right)}. \tag{7}$$

Here $\langle |S| \rangle$ is the magnitude of the resolved strain-rate tensor. The transport equations make use of two blending functions, F_1 and F_2, and two limiters. For details of these functions and the model constants see Section A.1.

2.2. Hybrid models

2.2.1. DDES

Delayed Detached Eddy Simulation (DDES) [13] is an adaptation of the Detached Eddy Simulation (DES) [3] model. The switch between RANS and LES is based on the turbulent length scale l_t and a shielding function f_d. The k transport equation becomes

$$\frac{\mathrm{D}k}{\mathrm{D}t} = P_k - \frac{k^{3/2}}{l_t} + \frac{\partial}{\partial x_j}\left((\nu + \nu_t \sigma_k)\frac{\partial k}{\partial x_j}\right), \tag{8}$$

including the turbulent length scale

$$l_t = l_t^{RANS} - f_d \max\left(l_t^{RANS} - l_t^{SRS}, 0\right). \tag{9}$$

The RANS and SRS length scales are defined as

$$l_t^{RANS} = \frac{\sqrt{k}}{\beta^* \omega} \quad \text{and} \quad l_t^{SRS} = C_{DDES}\Delta, \tag{10}$$

in which Δ is the maximum cell length. The coefficients and additional shielding function are given in Section A.2.

2.2.2. IDDES

In DDES the transition from RANS to LES inside a wall boundary layer is prohibited, which leads to a lack of resolved velocity fluctuations close to the wall. This can suppress dynamics in flow phenomena close to the wall, such as sheet cavitation. A different Hybrid model is Improved Delayed Detached Eddy Simulation (IDDES) [48], which aims to use DES as a Wall-Modelled LES (WMLES), while employing RANS in the near wall region instead of an analytical expression. Consequently IDDES is better able to handle separating flows, since LES is also allowed inside the boundary layer. A wall-normal resolution $y^+ = u_\tau y/\nu < 1$ at the wall is still required. In IDDES the blending is achieved by a different shielding function f_{dt}. Note that due to the different formulation, the model is prohibited to switch to RANS in the boundary layer and far field. This can therefore deteriorate the results on a coarse grid. The coefficients and auxiliary functions are given in Section A.3.

2.2.3. XLES

The final Hybrid model considered in this study is eXtra-Large Eddy Simulation (XLES) [15]. It is similar to DDES and IDDES, but with a switching function which is not dependent on the wall distance (which can be computationally expensive and difficult to define for a complex geometry). Furthermore, in LES mode a different

sub-filter stress model to DES is used (the KSGS model). The difference between RANS and LES modes lies in the definition of the eddy-viscosity and dissipation. For RANS these are given as

$$\nu_t = l\sqrt{k} \qquad \text{and} \qquad \epsilon = \beta_k \frac{k^{\frac{3}{2}}}{l}, \tag{11}$$

with $l = \sqrt{k}/\omega$, while for the LES sub-filter model

$$\nu_t = C_1 \Delta \sqrt{k} \qquad \text{and} \qquad \epsilon = C_2 \frac{k^{\frac{3}{2}}}{\Delta}, \tag{12}$$

with Δ defined as the maximum cell length. The RANS model is closed with a modified equation for ω, based on the $k-\omega$ TNT model [49],

$$\frac{\mathrm{D}\omega}{\mathrm{D}t} = P_\omega - \beta_\omega \omega^2 + \frac{\sigma_d}{\omega} \max\left(\frac{\partial k}{\partial x_i}\frac{\partial \omega}{\partial x_i}, 0\right) + \frac{\partial}{\partial x_j}\left((\nu + \sigma_\omega \nu_t)\frac{\partial \omega}{\partial x_j}\right), \tag{13}$$

with a production term

$$P_\omega = \alpha_\omega \langle S \rangle^2. \tag{14}$$

The switch between RANS and LES mode is made using a composite length scale $\tilde{l}$ defined as

$$\tilde{l} = \min(l, C_1 \Delta). \tag{15}$$

The coefficients and auxiliary functions are given in Section A.4.

2.3. Bridging model

The combination of RANS with LES in Hybrid models improves accuracy but may lead to commutation errors in the transition between the RANS and LES zones. An approach without commutation errors is the Bridging family of models, such as the Partially Averaged Navier-Stokes (PANS) model [2]. The PANS model is based on spatially filtering the Navier-Stokes equations, where the sub-filter stress tensor is modelled using a set of reformulated RANS equations including the modelled-to-total ratio of turbulence kinetic energy and dissipation rate,

$$f_k = \frac{k}{K} \qquad \text{and} \qquad f_\omega = \frac{\omega}{\Omega} = \frac{f_\epsilon}{f_k}. \tag{16}$$

The PANS model in this work is based on the $k-\omega$ SST model [47,50], with the transport equations

$$\frac{\mathrm{D}k}{\mathrm{D}t} = P_k - \beta^* \omega k + \frac{\partial}{\partial x_j}\left[\left(\nu + \nu_t \sigma_k \frac{f_\omega}{f_k}\right)\frac{\partial k}{\partial x_j}\right], \tag{17}$$

$$\frac{\mathrm{D}\omega}{\mathrm{D}t} = \frac{\alpha}{\nu_t} P_k - \left(P' - \frac{P'}{f_\omega} + \frac{\beta\omega}{f_\omega}\right)\omega + \frac{\partial}{\partial x_j}\left[\left(\nu + \nu_t \sigma_\omega \frac{f_\omega}{f_k}\right)\frac{\partial \omega}{\partial x_j}\right] + 2\frac{\sigma_{\omega 2}}{\omega}\frac{f_\omega}{f_k}(1 - F_1)\frac{\partial k}{\partial x_j}\frac{\partial \omega}{\partial x_j} \tag{18}$$

with

$$P' = \frac{\alpha \beta^* k}{\nu_t} \qquad \text{and} \qquad \nu_t = \frac{a_1 k}{\max(a_1 \omega, \langle S \rangle F_2)}. \tag{19}$$

For the auxiliary functions and constants see Section A.5.

In PANS, the closure is viscosity-based (the sub-filter viscosity is a function of the modelled flow field (k, ω)), whereas in LES the closure is grid-based (sub-filter viscosity is a function of the cut-off length scale (Δ)) [51]. Consequently, in contrast to LES, the cut-off length scale of the resolved flow is not predetermined in PANS. The physical resolution is only determined by the settings, which leads to an overlap between the PANS resolved and modelled spectra [51]. Since the grid remains fixed, computations with an f_k larger than what the grid allows are comparable to an explicitly filtered LES (although based on a different modelling framework). Computations with a very low f_k value are effectively an Implicit LES (under-resolved DNS).

The filtering depends only on the value of f_k and f_ϵ. f_k determines the physical resolution of the flow, f_ϵ determines the overlap between the energy-containing and the dissipation ranges. The effect of modifying f_ϵ is investigated in Klapwijk et al. [52], in which it was concluded that f_ϵ should be kept equal to 1.0 (also known as the 'high Reynolds number' approach), to avoid adding excessive dissipation. f_k and f_ϵ can either vary in space and/or time, or be kept constant throughout the domain and computation. The drawback of the first approach is that this entangles the modelling error and numerical error, and thereby destroys one of the key advantages of the PANS model. Although this approach is gaining popularity in literature, however there is no consensus on how f_k should be (a priori or dynamically) chosen [53]. Throughout this work a constant value for f_k is used.

2.4. LES

Large Eddy Simulation (LES) is founded on the principle that the larger scales of turbulence are resolved, while the smaller scales are modelled. In order to enable this, the filtering operation is performed spatially; either explicitly or implicitly (on the grid). To relate the sub-filter stress to the filtered strain rate, a number of models can be employed. In this work, a selection is made based on the most common models found in the open literature.

2.4.1. Smagorinsky

The Smagorinsky model [16] models the eddy-viscosity as

$$\nu_t = (C_s \Delta)^2 \langle |S| \rangle, \tag{20}$$

with $\langle |S| \rangle = \sqrt{2\langle S_{ij} \rangle \langle S_{ij} \rangle}$ and a model constant C_s. The model constant depends on the flow and in literature values in the range $0.065 - 0.23$ are found. In this paper a value of 0.10 is applied. The filtering is done implicitly, using the filter as defined by Smagorinsky:

$$\Delta = (\Delta_x \Delta_y \Delta_z)^{\frac{1}{3}}. \tag{21}$$

In the case of highly anisotropic cells, which occur often near walls, this filter is too optimistic leading to an underpredicted eddy-viscosity.

2.4.2. Lilly

To circumvent difficulties in obtaining a general constant for the Smagorinsky model and to improve behaviour near walls, Germano et al. [17] suggested using a constant which varies in time and space, thereby adapting to the resolved scales. Lilly [18] applied a least-squares estimate to obtain the constant, known as the Lilly Model. In this approach, next to the spatial filter a second, coarser, filter is applied. This filter, known as the 'test' filter, indicated by $\widehat{\cdot}$, is usually defined as $\widehat{\Delta} = 2\Delta$. The sub-test filter stress, T_{ij}, is defined analogously to the sub-filter stress, that is

$$T_{ij} - \frac{1}{3}\delta_{ij} T_{kk} = 2\left(C_s \widehat{\Delta}\right)^2 \widehat{\langle |S| \rangle \langle S_{ij} \rangle}. \tag{22}$$

The model constant is obtained using

$$C_s = \frac{1}{2}\frac{L_{ij} M_{ij}}{M_{ij} M_{ij}}, \tag{23}$$

in which the error between the resolved scales of motion L_{ij} and the local closure M_{ij} is minimised. L_{ij} is defined as the difference between the sub-filter stress on the normal filter (τ_{ij}) and on the test-filter level,

$$L_{ij} = T_{ij} - \widehat{\tau_{ij}} = -\widehat{u_i u_j} + \widehat{\langle u_i \rangle}\,\widehat{\langle u_j \rangle}, \tag{24}$$

and M_{ij} is defined as

$$M_{ij} = \widehat{\Delta}^2 \widehat{\langle|S|\rangle \langle S_{ij}\rangle} - \Delta^2 \langle \widehat{|S|} \rangle \langle \widehat{S_{ij}} \rangle. \tag{25}$$

A downside of this model is that the model requires spatial averaging of the constant to reduce the variability in space and time, else the value of C_s can become either negative or unphysically large [54]. Since this is often not possible for industrial flow cases due to the absence of flow homogeneity, the constant is bounded between 0 and 10 times the upper limit of the Smagorinsky constant as found in literature, so $C_s \in [0, 2.3]$.

2.4.3. WALE

The Wall Adaptive Local Eddy-viscosity (WALE) model by Nicoud and Ducros [19] was proposed for LES in complex geometries to account for the effects of the strain and rotation rate of the smallest resolved velocity fluctuations. It should also recover proper near-wall scaling for the eddy-viscosity without dynamic procedures. The sub-filter viscosity is determined as

$$\nu_t = L_s^2 \frac{\left(S_{ij}^d S_{ij}^d\right)^{3/2}}{\left(\langle S_{ij}\rangle \langle S_{ij}\rangle\right)^{5/2} + \left(S_{ij}^d S_{ij}^d\right)^{5/4}}, \tag{26}$$

based on the square of the velocity gradient tensor

$$S_{ij}^d = \frac{1}{2}\left(\langle g_{ij}\rangle^2 + \langle g_{ji}\rangle^2\right) - \frac{1}{3}\delta_{ij}\langle g_{kk}\rangle^2 \tag{27}$$

with

$$\langle g_{ij}\rangle = \frac{\partial \langle U_i\rangle}{\partial x_j}. \tag{28}$$

The length scale is given as

$$L_s = \min\left(\kappa d, C_s \Delta\right) \tag{29}$$

in which d indicates the wall distance and $\kappa = 0.41$.

2.4.4. KSGS

The final sub-filter model is the k sub-grid Stress (KSGS) model [20], for which a transport equation for the sub-filter turbulence kinetic energy (Eq. 5) is solved, with the production term defined as

$$P_k = \nu_t \langle S\rangle^2. \tag{30}$$

The eddy-viscosity and dissipation terms are defined in Eq. 12.

2.4.5. ILES

An alternative approach to LES sub-filter modelling is known as Implicit LES (ILES) [55]. Instead of applying a sub-filter model, it is assumed that the added numerical diffusion due to the use of coarse(r) grids and low order (upwinding) schemes acts as a sub-filter model. Whilst an attractive approach due to low computational cost (no sub-filter model is required), caution is needed in employing this approach, especially in resolving structures near the presumed cut-off scale [56]. Due to the absence of a sub-filter model, the only contributing factor in the ratio of modelled-to-total kinetic energy is the grid. As a consequence making a proper grid becomes even more important than usual; the reliability of ILES for industrial flow cases on highly non-uniform, anisotropic grids can lead to large errors. The filter length varies significantly in the domain, and due to the anisotropic cells, the numerical dissipation due to the convection scheme varies in different directions. Secondly, the application of low order (upwinding) methods using coarse grids can lead to too much added dissipation, thereby not capturing finer structures [56]. Finally, the results are even more grid dependent than for normal LES, which makes proper solution verification impossible. Nevertheless it is a widely employed approach, and is therefore also included in this work.

2.5. Turbulence generating methods

As shown in the literature, the use of scale-resolving turbulence methods for a turbulent channel yields a so-called supercritical laminar solution for which many flow-through times are needed to trigger transition to the turbulent regime [31]. To this end in the current work two methods are employed to speed up the transition. For cases with streamwise periodic boundary conditions (see Section 3) the method suggested by Schoppa and Hussain [57] is used as reported in Klapwijk et al. [58]. This method is only applicable to cases with streamwise periodic boundary conditions, and is tuned for a turbulent channel flow. It is therefore not a general approach.

Secondly, a more general method, which does not depend on streamwise periodic boundary conditions, is applied. Synthetic turbulence is generated using a modified version of the digital filter method by Xie and Castro [36]. This method is more general, and does not require flow recycling. In the current implementation the method is able to generate anisotropic, inhomogeneous turbulence which is sufficient for most industrial applications such as the flow around wings, propellers, ship hulls, etc. In the method random numbers, $r_{m,l,i}$, with zero mean and unit variance, are generated on a Cartesian grid at each time step. Here m, l indicate the position indices and i the velocity component. These numbers are spatially correlated using

$$\psi_{m,l,i} = \sum_{j=-N}^{N} \sum_{k=-N}^{N} b_j b_k r_{m+j,l+k,i}, \tag{31}$$

after which they are temporally correlated with the numbers generated at the previous time step using

$$\Psi_i(t) = \Psi_i(t - \Delta t) \exp\left(-\frac{\pi \Delta t}{2T}\right) + \psi_i(t)\left[1 - \exp\left(-\frac{\pi \Delta t}{2T}\right)\right]. \tag{32}$$

Here $T = I_i/\overline{U_i}$ is the Lagrangian time scale and b_j and b_k are filter coefficients used to generate spatial correlations, and are defined as

$$b_j = \frac{b'_j}{\left(\sum_{l=-N_j}^{N_j} b'^2_l\right)} \quad \text{and} \quad b_k = \frac{b'_k}{\left(\sum_{m=-N_k}^{N_k} b'^2_m\right)}, \tag{33}$$

with

$$b'_j = \exp\left(-\frac{\pi |j|}{2n}\right) \quad \text{and} \quad b'_k = \exp\left(-\frac{\pi |k|}{2n}\right). \tag{34}$$

The spatially and temporally correlated numbers are transformed to velocity fluctuations using

$$U'_i = a_{ij} \cdot \Psi_i \tag{35}$$

in which a_{ij} indicates the Lund transformation matrix, which is based on a Cholesky decomposition of the Reynolds stress tensor R_{ij} [10],

$$a_{ij} = \begin{bmatrix} \sqrt{R_{11}} & 0 & 0 \\ R_{11}/a_{11} & \sqrt{R_{22} - a_{21}^2} & 0 \\ R_{31}/a_{11} & (R_{32} - a_{21}a_{31})/a_{22} & \sqrt{R_{33} - a_{31}^2 - a_{32}^2} \end{bmatrix}. \tag{36}$$

In the current work a string of pseudo-random numbers is employed, i.e. the same range of random numbers for every computation. For more details the reader is referred to Xie and Castro [36] and [39]. In these works the velocity is modified directly inside the first non-linear PISO loop, either at the inflow, or in the domain. In the current work the velocity fluctuations are

transformed to a body-force term in the momentum equations, explicitly added on the right hand side of the equations. This is done to improve iterative convergence and mass conservation. The transformation is achieved using

$$F_{b,i} = \frac{\left(U_{i,inflow} + U_i' - U_i\right)\rho\overline{U_i}}{L_{tg}} \cdot b \tag{37}$$

where $U_{i,\ inflow}$ is the mean velocity as defined at the generator plane, U_i' comes from Eq. 35 and U_i is the instantaneous velocity in a cell, obtained from the solver at the current non-linear loop. L_{tg} indicates the distance in the flow direction over which the body-force term is applied, and b is an arbitrary multiplication factor to increase the convergence of the velocity towards the desired fluctuations. For now b is taken as 300. Notice that this body-force term goes to zero when the local velocity equals the desired mean plus fluctuation.

3. Numerical setup and solver

Computations are made using a rectangular domain, with two no-slip walls oriented normal to the y-direction and periodic boundary conditions in spanwise direction. (see Fig. 2). The remaining boundaries are either connected using periodic boundary conditions in order to approximate an infinite channel; or alternatively, an inflow and outflow boundary condition is specified if a synthetic turbulence generator is applied. Cartesian grids with hyperbolic tangent clustering towards the walls are used, as described in Section 4.3. The non-dimensional time step for the grid used for comparing turbulence modelling approaches, *G4*, is $\Delta t^* = 1/2u_\tau \Delta t/\delta \approx 1 \times 10^{-3}$. This leads to $\Delta t^+ = u_\tau^2 \Delta t/\nu \approx 0.08$ and a maximum Courant number below 0.2 (2000 time steps per flow-through time). To maintain the proper bulk and friction Reynolds numbers, $Re_b = U_b 2\delta/\nu$ and $Re_\tau = u_\tau \delta/\nu$ respectively, a body-force is applied which is proportional to the streamwise pressure gradient $\mathrm{d}p/\mathrm{d}x = -\tau_w/\delta$, with $\tau_w = \rho u_\tau^2$ [59].

The numerical solver used for all simulations in this work is ReFRESCO [60], a multiphase unsteady incompressible viscous flow solver using RANS and Scale-Resolving Simulation models, complemented with cavitation models and volume-fraction transport equations for different phases. For the simulations reported here work time integration is performed using a second-order implicit three time level scheme, and the convection terms in the momentum equations are discretised using a second-order accurate central differencing scheme (the Péclet number has a magnitude of $\mathcal{O}(10)$). An investigation into the effect of the convection scheme for the momentum equation can be found in Section 4.3. The turbulence equations are discretised using a first-order upwind scheme. Due to the fine grid resolution employed, the effect of discretisation on the sub-filter stresses is limited.

4. Numerical errors

As generally accepted, numerical errors can be divide into input, round-off, iterative, discretisation, and, in the case of unsteady computations, statistical errors [61]. The input error is assumed to be negligible due to the well controlled conditions in the computations, and either the periodic nature of the solution, or the reliability of the DNS results reported in the open literature. The round-off error is negligible due to the use of double precision arithmetic. Therefore, in this work, only the iterative, discretisation and statistical error are assessed.

The results are obtained along a line perpendicular to the wall at the centre of the channel (see Section 4.2). Computations are performed using grid *G4* (see Section 4.3) and using PANS ($f_k = 0.10$) unless indicated otherwise. Only half the channel height is shown.

4.1. Iterative error

The iterative convergence is assessed based on the residuals, normalised by the diagonal element of the left-hand-side matrix of the linear system of equations. This is of particular interest since if the iterative error would be of the same order of magnitude as the turbulence fluctuations, the results would be strongly affected. Despite this, the influence of iterative error is rarely studied in the open literature. Following the approach advocated by Eça et al. [62], a PANS computation with $f_k = 0.10$ was performed using different iterative convergence criteria ($L_2 = 10^{-3}$, 10^{-4}, 10^{-5}, 10^{-6}, 10^{-7} and 10^{-8}). The effect on the mean velocity ($\overline{u}^+$), Reynolds stresses ($Re_{ij} = \overline{u_i' u_j'}/u_\tau^2$) and turbulence kinetic energy spectra ($E_u(f)$ at $y^+ \approx 20$) along a wall-normal line at the centre of the domain is shown in Fig. 3. For values of $L_2 = 10^{-3}$ and 10^{-4}, the mean velocity shows an underprediction in the buffer layer ($5 < y^+ < 30$), while for $L_2 \leq 10^{-5}$ the results are converged. The Reynolds stresses and spectra also show a large mismatch with the reference data for $L_2 = 10^{-3}$ and 10^{-4}. The magnitude of the peak value Re_{uu} and the turbulence kinetic energy spectra converge for stricter convergence criteria. As a compromise between cost and accuracy, the criterium $L_2 = 10^{-6}$ is used in the remainder of this work. Applying this criterium leads to a residual of $L_\infty = 10^{-5}$ in each time step for momentum; the residuals for pressure and turbulence equations are at least one order of magnitude smaller. In this manner, the iterative error is smaller than the turbulence fluctuations of interest.

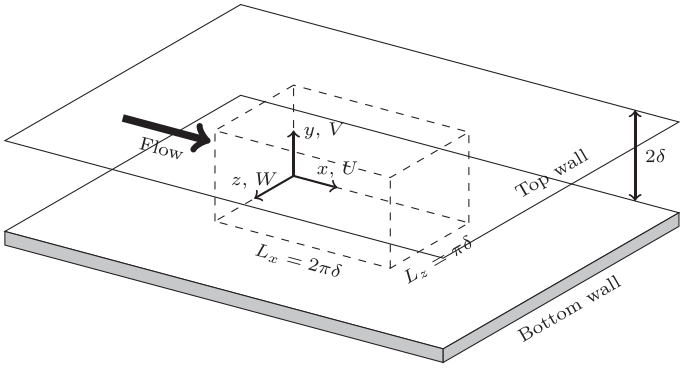

Symbol	Value
δ [m]	0.1
U_b [m/s]	6.928×10^{-2}
u_τ [m/s]	3.966×10^{-3}
τ_w [N/m^2]	1.570×10^{-1}
ν [m^2/s]	1.004×10^{-6}
Re_τ	395
Re_b	13 800

Fig. 2. Schematic overview of the domain and physical parameters. The dashed lines indicate the computational domain. The figure is based on the drawing of de Villiers [31].

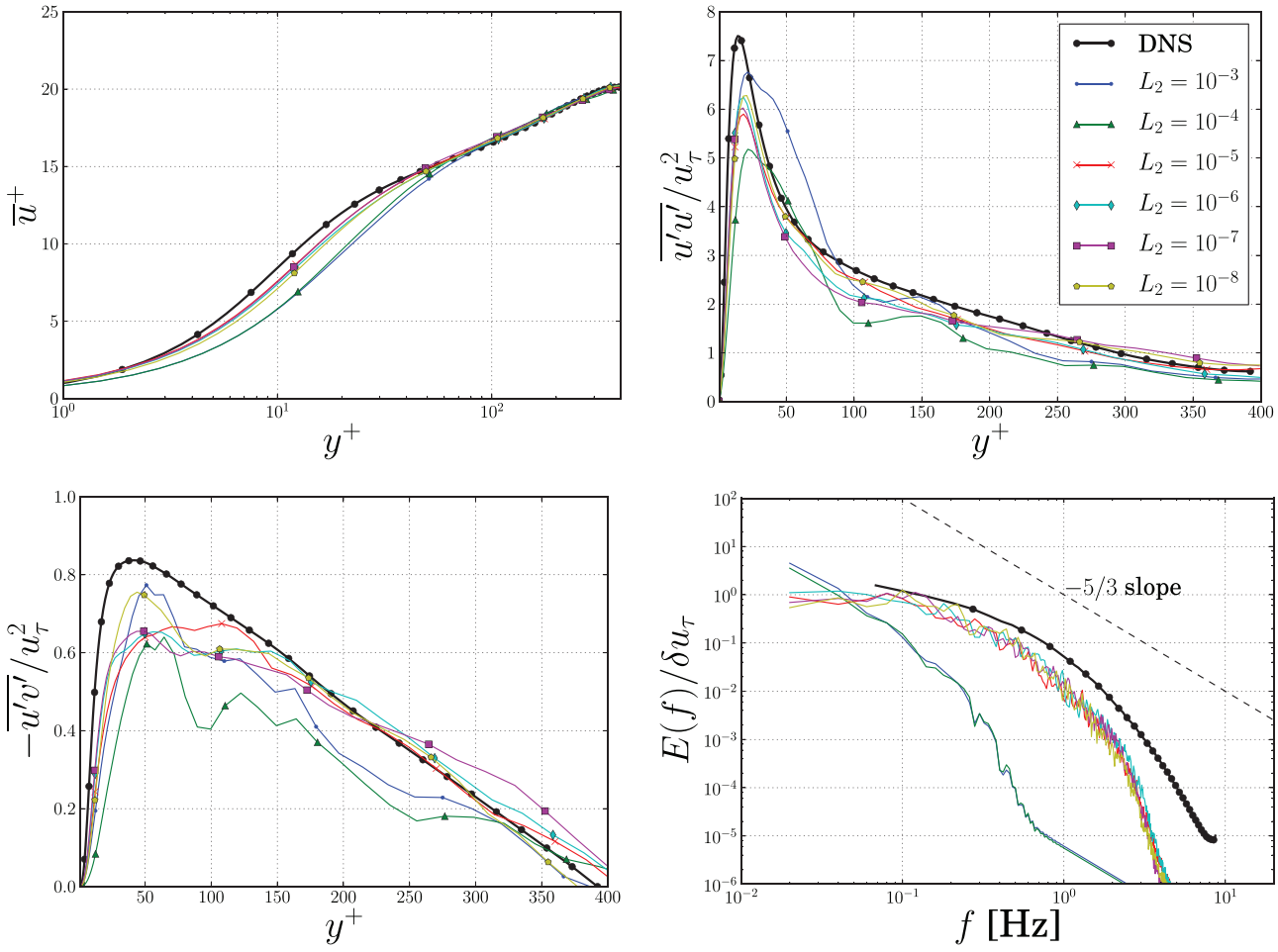

Fig. 3. Mean velocity ($\overline{u}^+$) profiles, Reynolds stress (Re_{uu} and Re_{uv}) profiles and turbulence kinetic energy spectra ($E_{u,y^+\approx 20}(f)$) using different iterative convergence criteria.

4.2. Statistical error

A potentially dominating error in unsteady and especially turbulence resolving simulations is the statistical error. In order to remove the start-up effects and estimate the magnitude of this source of uncertainty, the Transient Scanning Technique (TST) is employed [63]. This technique allows an estimation of the statistical uncertainty based on a signal of finite length. The uncertainty is expanded to obtain a 95% confidence interval. The TST is applied to the velocity signals and Reynolds stresses at measurement points along the height of the channel. Based on the TST, it is found that the first 11 flow-through times ($\approx$30000 time steps) must be removed to eliminate the start-up effects. This conclusion is independent of the wall-normal distance of the measurement point. In the remainder of this work, the mean values are then computed based on approximately 45 flow-through times, resulting in a statistical uncertainty for the mean streamwise velocity below 2%, and for the Reynolds stress components below 10%.

These uncertainties are in agreement with the sampling errors as obtained from the engineering approaches suggested by Ries et al. [64]. The estimates of the sampling error e for $\overline{u}^+$, u' and u'^2_{rms} are given as:

$$e = \sqrt{\frac{2\delta I^2}{U_b t_{av}}}, \qquad e = \sqrt{\frac{\delta}{U_b t_{av}}} \qquad \text{and} \qquad e = \sqrt{\frac{4\delta}{U_b t_{av}}}. \tag{38}$$

Here t_{av} indicates the averaging time and I the turbulence intensity $I = u'/\overline{u}$. These estimates give sampling errors of 1%, 5% and 10% for $\overline{u}$, u' and u'^2 respectively when applied to the results of the present study.

In order to reduce these errors more flow-through times should be computed. It must be noted that in literature spatial averaging is often applied to the results since the flow is statistically homogeneous [64]. In this way a low statistical uncertainty is achieved using fewer flow-through times. However this implies that the flow is statistically converged in the entire domain, but not at every location. In this work spatial averaging is explicitly not applied, to ensure a statistically converged solution at all locations, and to properly compare with results obtained with a synthetic turbulence generator.

4.3. Discretisation error

In order to assess the discretisation error, four different grids (with refinement ratios $r_i = h_i/h_1 = \Delta t_i/\Delta t_1 = 1.00$, 1.25, 1.57 and 1.97) were employed. Details of the grids are given in Table 1. The grid designated *G4* is equal to the one used for the DNS reference data [28]. Note that all these grids are well within LES guidelines, in terms of wall resolution, found in literature, and have resolutions typical of DNS [56,65]. It is commonly assumed in literature, when grids with DNS resolution, in conjunction with second-order schemes, are used for LES, that discretisation errors are negligible and do not have to be assessed. However, discretisation errors depend on both the number of cells and the accuracy of the schemes employed, and assessment of these errors is still necessary.

Table 1
Details of used grids. r_i $(= h_i/h_1 = \Delta t_i/\Delta t_1)$ indicates the refinement ratio, N the number of cells in different directions, Δy_1 the initial wall-normal spacing, $x^+ = u_\tau x/\nu$, $y^+ = u_\tau y/\nu$ and $z^+ = u_\tau z/\nu$ the average non-dimensional wall units in different directions and the maximum Courant number, $Co_{\max}$.

Grid	r_i	N_x	N_y	N_z	$N/10^6$	$\Delta y_1 \cdot 10^4$	x^+	y^+	z^+	$Co_{\max}$
G6	3.97	63	47	47	0.14	2.1	24	0.2	20	0.07
G5	2.63	95	71	71	0.48	1.4	16	0.13	13	0.12
G4	**1.95**	**127**	**95**	**95**	**1.18**	**1.0**	**12**	**0.10**	**10**	**0.20**
G3	1.56	159	119	119	2.30	0.8	9.6	0.08	8	0.21
G2	1.25	199	149	149	4.50	0.6	7.7	0.06	6.4	0.22
G1	1.0	249	187	187	8.84	0.5	6.1	0.05	5.1	0.25

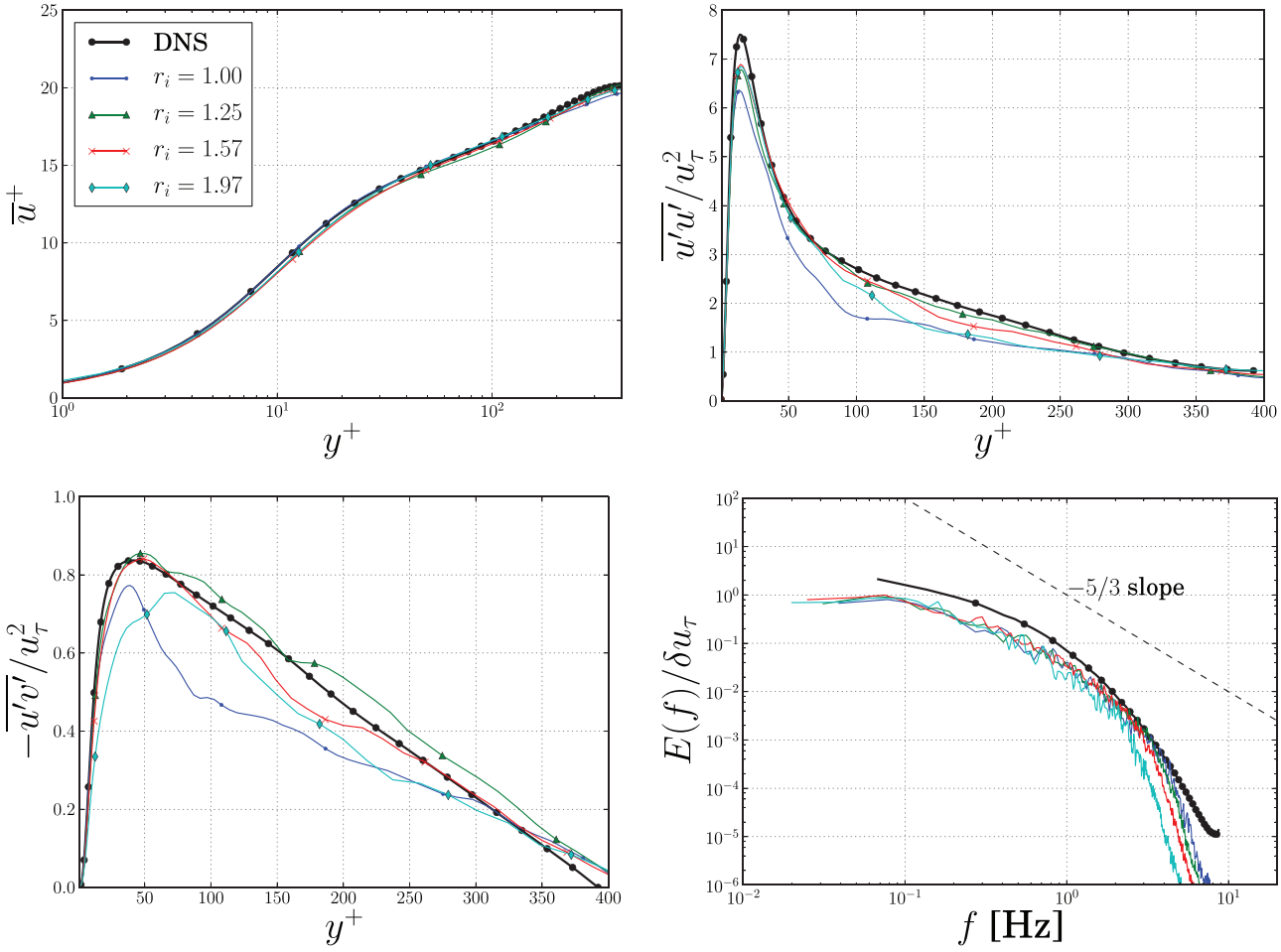

Fig. 4. Mean velocity ($\overline{u}^+$) profiles, Reynolds stress (Re_{uu} and Re_{uv}) profiles and turbulence kinetic energy spectra ($E_{u,y^+\approx 20}(f)$) using different grids and PANS ($f_k = 0.10$).

The effect of grid refinement is shown in Fig. 4. Both the mean velocity and Reynolds stresses appear reasonably insensitive to grid resolution, however Re_{uu} and Re_{uv} deviate slightly on the finest grid. The main differences are observed for the turbulence kinetic energy spectra. Grid refinement leads to a slightly increased cut-off frequency, since the smaller cells allow for higher wavenumbers to be resolved. This indicates that the employed f_k (0.10) is below the grid cut-off, i.e. the grid and numerical settings do not result in DNS resolution. Nevertheless, based on the similarity between the results it is concluded that the coarsest grid has a sufficient resolution. For this reason, grid refinement for the LES models was not pursued, since due to the fine grid resolution, little effect of the sub-filter model is expected. Instead, to compare the effect of grid resolution on the sub-filter modelling, grid coarsening was performed. To this end, two additional grids (with refinement ratios $r_i = 2.63$ and 3.97) are employed, in combination with PANS ($f_k = 0.10$), LES KSGS and ILES. Fig. 5 shows that even the coarsest grid still has sufficient resolution to predict the mean velocity profiles well, in the cases of PANS and ILES. For Re_{uu} both ILES and PANS overpredict the peak near the wall, especially on coarser grids. This overprediction is absent for LES KSGS, due to the sub-filter model. On finer grids however, the peak is underpredicted, indicating that the SGS is too dissipative. The peak on the coarsest grid is also shifted away from the wall. For Re_{uv}, again LES KSGS predicts the magnitude better on a coarse grid than ILES and PANS. This difference is absent on finer grids. In terms of turbulence kinetic energy spectra, it is clear that grid refinement leads to an increase in energy at higher frequencies, i.e. the cut-off frequency increases. The effect of the sub-filter model is also clear for LES KSGS, the cut-off on all grids being at a lower frequency than for ILES and PANS. This effect is most significant on the coarsest grid.

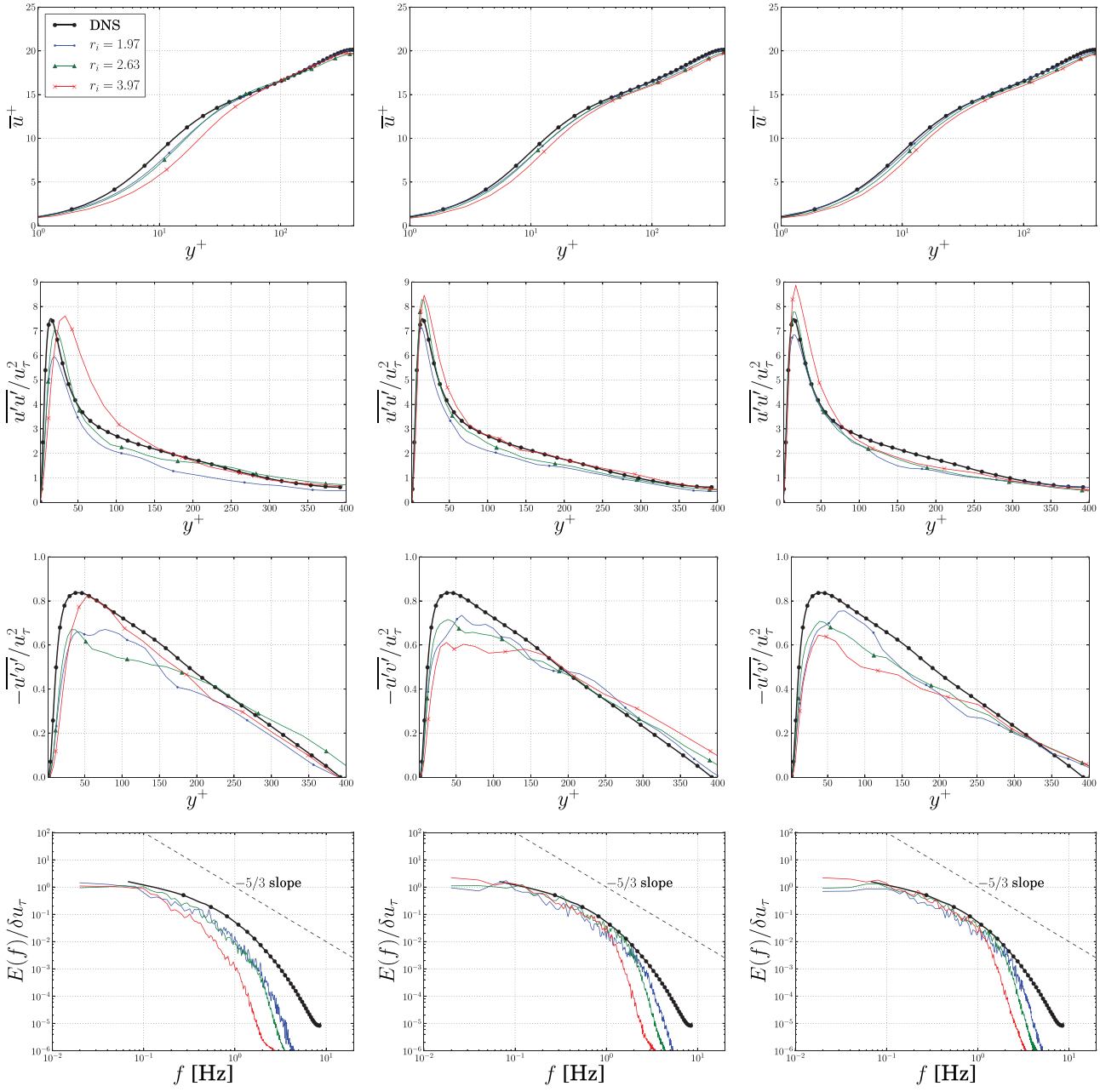

(a) LES KSGS (b) ILES (c) PANS ($f_k = 0.10$)

Fig. 5. Mean velocity ($\overline{u}^+$) profiles, Reynolds stress (Re_{uu} and Re_{uv}) profiles and turbulence kinetic energy spectra ($E_{u,y^+\approx 20}(f)$) using different grids.

To conclude, the grid designated *G4* has a sufficient resolution to be able to compare the different models. Grid coarsening shows that, although the results obtained by ILES appear reasonable, the absence of a sub-filter model can lead to an overprediction of turbulent stresses on coarse grids. In addition, similarity in results indicates that PANS with a low f_k is comparable to LES without a sub-filter model (ILES).

A second source of discretisation error is the discretisation of the convection terms in the equations. Due to the usage of a unstructured Finite Volume CFD code, we are limited to second-order accurate schemes. For the Reynolds number studied here, the discretisation of the momentum equations is dominant. Basara et al. [66] investigated blended upwind-CD schemes for Finite Volume LES and Hybrid methods. They state that 'results obtained with a blending factor lower than 0.98 or 0.96 are treated as suspicious', and that the use of a second-order accurate Central-Differencing scheme is preferred. However in industrial high Reynolds number flows this is often not possible, meaning that (lower-order) upwinding, or blended schemes are used [66]. In order to investigate this effect, the convection scheme for the momentum equation is varied between First Order Upwind (FOU), Central Differencing (CD), a blended upwind-CD with a blending factor of 0.5 (FOU-CD) and the approximately second-order QUICK (Quadratic Upstream Interpolation for Convective Kinematics) scheme. The investigation is performed for ILES, LES KSGS and PANS with $f_k = 0.10$. The computations are deliberately performed on the coarser grid *G6* to highlight the difference between different convection schemes and different sub-filter models [66]. These differences are

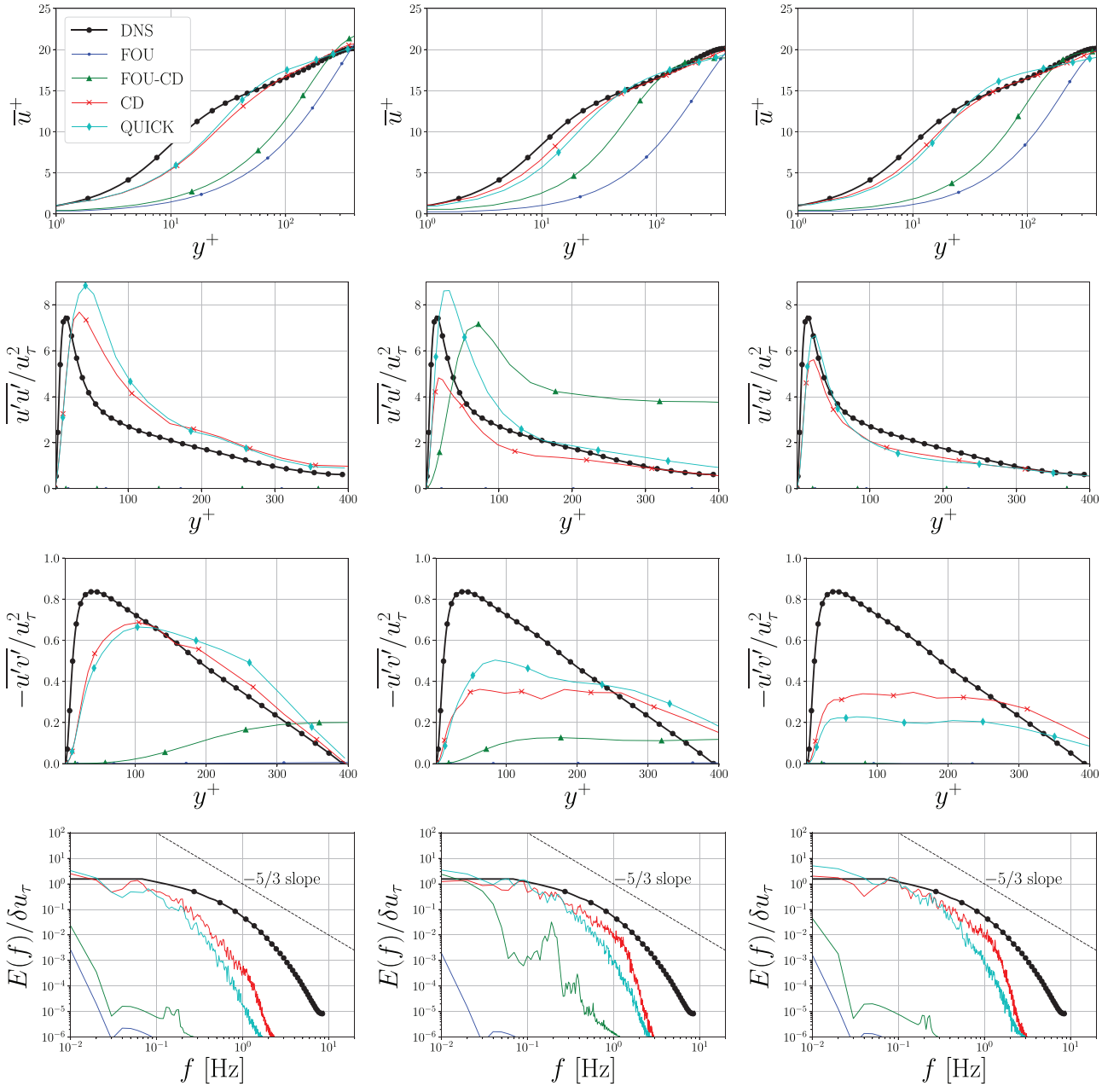

(a) LES KSGS (b) ILES (c) PANS ($f_k = 0.10$)

Fig. 6. Comparison of normalised mean velocity ($\overline{u}^+$), Reynolds stress (Re_{uu}) profiles and turbulence kinetic energy spectra ($E_{u,y^+\approx 20}(f)$) using different convection schemes for the momentum equations.

expected to be smaller on finer grids. The non-dimensional time step $\Delta t^* = u_\tau \Delta t/2\delta \approx 2 \times 10^{-3}$ leads to $\Delta t^+ = u_\tau^2 \Delta t/\nu \approx 0.5$ and a maximum Courant number of 0.1.

Fig. 6 shows the normalised mean velocity ($\overline{u}^+$) and Reynolds stress profiles (Re_{uu} and Re_{uv}), together with the turbulence kinetic energy spectra $E(f)$. In terms of velocity profiles, the CD scheme yields the best match with the reference data for all turbulence approaches. The QUICK scheme captures the trend, but overpredicts the velocity in the range $0.1 < y/\delta < 0.4$ and underpredicts the velocity in the outer layer ($y^+ > 50$), especially for the PANS model. FOU clearly yields a laminar, parabolic, velocity profile. Both the mean velocity and Reynolds stresses indicate that FOU and FOU-CD yield no fluctuations, i.e. a laminar flow; CD and QUICK yield a turbulent solution. Generally the magnitude of the Reynolds stresses are larger for QUICK than for CD. Finally the spectra are compared. Due to the laminar flow predicted using FOU and FOU-CD the energy contained in the spectrum is much lower for all models. Both CD and QUICK show the correct shape, but for all models CD contains more energy across the entire frequency range. There appears to be little difference between ILES and PANS. The spectrum for LES KSGS shows a cut-off at a lower frequency, since part of the turbulence is modelled by the sub-filter model.

To conclude it is clear that for all SRS, first order schemes add too much discretisation error and lead to a mismatch in flow profile. Fully second-order schemes yield the best results, while using QUICK (a commonly used scheme in industrial applications), reasonable results are obtained. With a QUICK scheme less energy is resolved than by the CD scheme, which is in line with literature

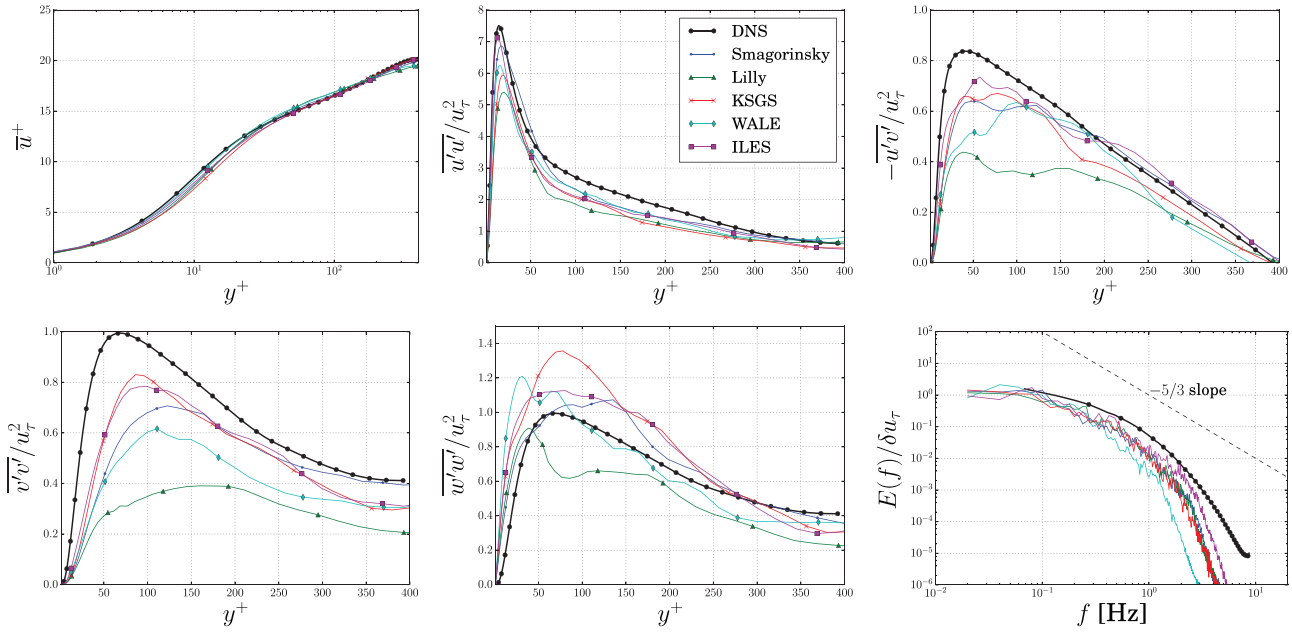

Fig. 7. Normalised mean velocity and Reynolds stress profiles and turbulence kinetic energy spectra using LES and DNS [28]. From left to right, and top to bottom $\overline{u}^+$, Re_{uu}, Re_{uv}, Re_{vv}, Re_{ww} and $E_{u,y^+\approx 20}(f)$.

[35,67]. In the remainder of this work the convection terms in the momentum equation are discretised using a second-order accurate CD scheme. For industrial cases the application of CD is typically not possible, due to high local cell Péclet numbers [68], although reasonable results can still be obtained using QUICK.

5. Comparison of turbulence approaches with streamwise periodic boundary conditions

5.1. LES

Fig. 7 shows the mean velocity profiles, Reynolds stresses and turbulence kinetic energy spectra of the streamwise velocity at $y^+ \approx 20$. The mean velocity profiles for all models capture the trend of the DNS data. In terms of Reynolds stresses, it is clear that all models capture the trend, but deviate in terms of magnitude. The highest Reynolds stress terms are generally obtained for the ILES and KSGS, followed by the Smagorinsky, Lilly and WALE model. The Lilly model performs adequately for Re_{uu}, but underpredicts Re_{uv}, Re_{vv} and Re_{ww}. For all models the magnitude of the Reynolds stress terms is generally underpredicted, with Re_{ww} an exception. For Re_{vv}, the peak is shifted towards the right for all models indicating that the strongest turbulence fluctuations occur further from the wall. The turbulence kinetic energy spectra for the LES models are comparable, although as shown in Section 4.3 this is grid dependent. For the resolution employed here, there is little difference between the models. Only ILES shows a slightly higher cut-off frequency due to the absence of a sub-filter model. Generally it appears that ILES yields the best results, which has been observed before for a channel flow on a fine grid. This is related to excessive diffusion and non-monotonic grid convergence for LES, i.e. on fine grids ILES can give better results than LES with a sub-filter model [69,70].

Turbulent structures in the flow are visualised in Fig. 8, using isocontour plots of Q, based on the instantaneous flow field. Q is defined as $Q = 1/2(|\langle\Omega\rangle| - |\langle S\rangle|)$, with $\langle\Omega\rangle$ defined as the anti-symmetric part of ∇u, representing local flow rotation [71]. The isocontours and the sides of the domain are coloured by the normalised streamwise velocity ($u^* = u/U_b$). Based on a visual observation, it appears that the Lilly and WALE model predict larger structures than the other models. For the Lilly model, this is related to the application of the 'test' filter, which is larger than the grid size; for the WALE model, this is a result of the inclusion of wall distance in the determination of the length scale L_s.

To conclude, the comparison shows that the best match for the Reynolds stresses is obtained with ILES, although this is strongly

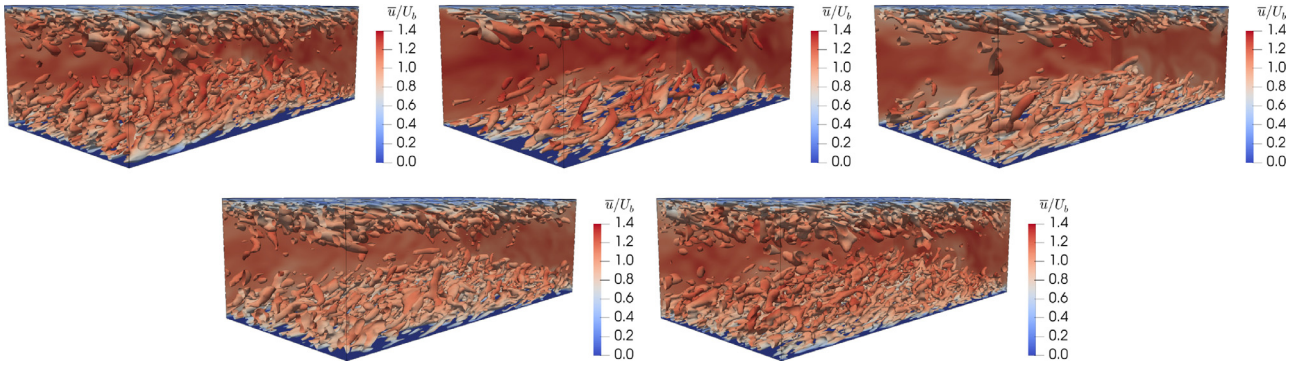

Fig. 8. LES instantaneous turbulent flow fields ($Q = 0.3$), coloured by $u^* = u/U_b$. First row from left to right Smagorinsky, Lilly and WALE, second row KSGS and ILES.

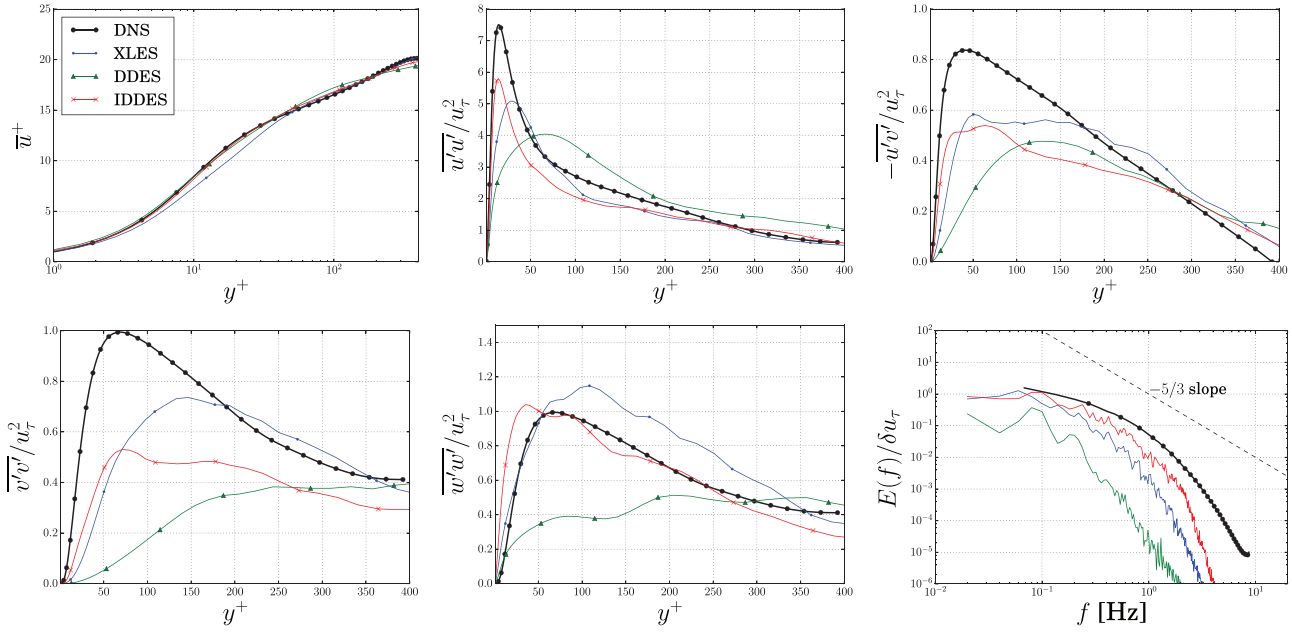

Fig. 9. Normalised mean velocity and Reynolds stress profiles and turbulence kinetic energy spectra using Hybrid models and DNS [28]. From left to right, and top to bottom $\overline{u}^+$, Re_{uu}, Re_{uv}, Re_{vv}, Re_{ww} and $E_{u,y^+\approx 20}(f)$.

grid dependent. Smagorinsky, KSGS and WALE perform comparably, and the Lilly model shows the poorest performance due to the larger test filter. The WALE model should perform better for flows involving complex geometries, meaning its advantages do not show up here.

5.2. Hybrid models

Fig. 9 shows the flow field statistics for the Hybrid models. For the mean velocity, XLES shows an underprediction in the buffer-layer ($5 \leq y^+ \leq 30$). DDES shows an overprediction in the log-law region and an underprediction near the centreline. IDDES matches the reference data well. In terms of Reynolds stresses, XLES captures the trend but underpredicts the magnitude for all components. The peak in the Re_{vv} and Re_{ww} distribution is significantly shifted away from the wall, an indication of the hybrid nature of the model. The DDES model has a more interesting behaviour. The shielding function of the model is formulated such that close to the wall, inside the boundary layer, RANS should be used. In the far field LES should be employed, with the RANS model acting as sub-filter model [32]. Since a turbulent channel flow consists solely of a boundary layer, with no far field region, one might expect the solution to be fully RANS. This explains the good match for the averaged velocity. However the Reynolds stress components show that turbulence is fully modelled only in the region $y^+ < 50$, while closer to the centre turbulence is resolved. The employed grid resolution leads to $l_t^{SRS} < l_t^{RANS}$, thereby forcing the switch to occur inside the boundary layer. The division between RANS and LES regions, is visible in Fig. 10. Note that even though this is the same behaviour which lead to the development of DDES as a replacement of DES, this can still occur for DDES under certain circumstances (i.e. combinations of test case and grid density). An effect of using LES only close to the centreline is an underprediction of the energy contained in the spectrum at the investigated location ($y^+ \approx 20$). In IDDES and XLES, the RANS region is much smaller (see Fig. 10), which is reflected in the magnitude of the Reynolds stresses. Due to the use of RANS close to the wall an underprediction occurs in this region. For IDDES and XLES models the turbulence kinetic energy spectrum also matches well with the other

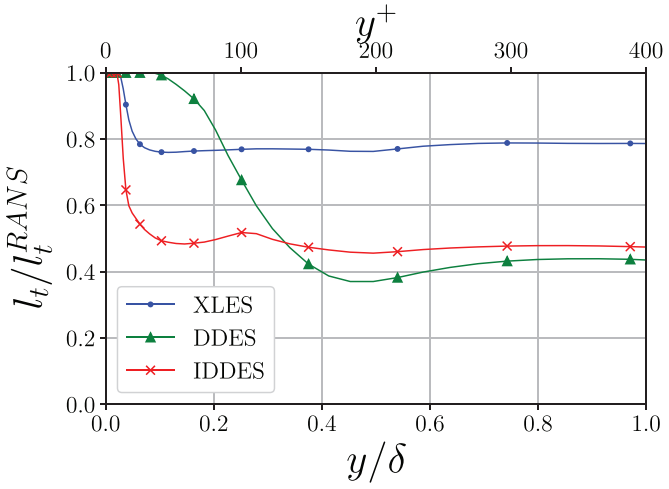

Fig. 10. Instantaneous, spatially averaged, LES regions (l_t/l_t^{RANS}) for the DDES and IDDES model (right). 1 indicates RANS, 0 LES.

LES results. Note that the underprediction for DDES is related to the location of the probe ($y^+ \approx 20$), which is inside the RANS layer. The fluctuations at this point are LES fluctuations which influence the RANS layer. The turbulence kinetic energy spectrum match the DNS data better for spectra closer to the centreline (not shown in this paper).

The turbulent structures in the flow are visualised in Fig. 11. The effect of using RANS near the walls in the DDES formulation is obvious, only larger structures in the centre of the channel exist. The structures in the IDDES and XLES model are similar to the LES Smagorinsky, KSGS and ILES results.

The results indicate that for cases where the instantaneous near wall flow field is of importance (for instance sheet cavitation), Hybrid models are less suitable than LES or PANS. DDES is not able to properly resolve the boundary layer. In contrast, IDDES performs better for the mean velocity and Reynolds stresses but with the exception of Re_{vv}. XLES underpredicts the all components of the Reynolds stress tensor.

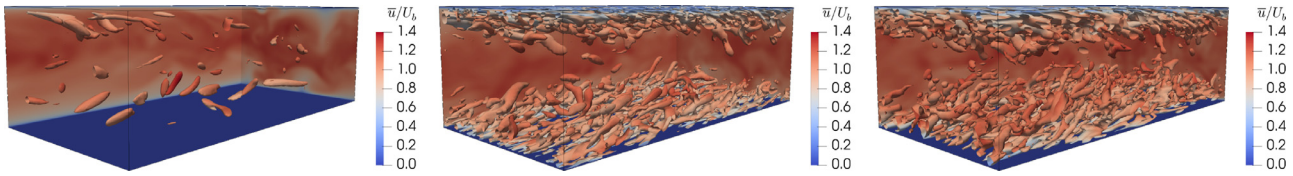

Fig. 11. Hybrid models instantaneous turbulent flow fields ($Q = 0.3$), coloured by $u^* = u/U_b$. From left to right DDES, IDDES and XLES.

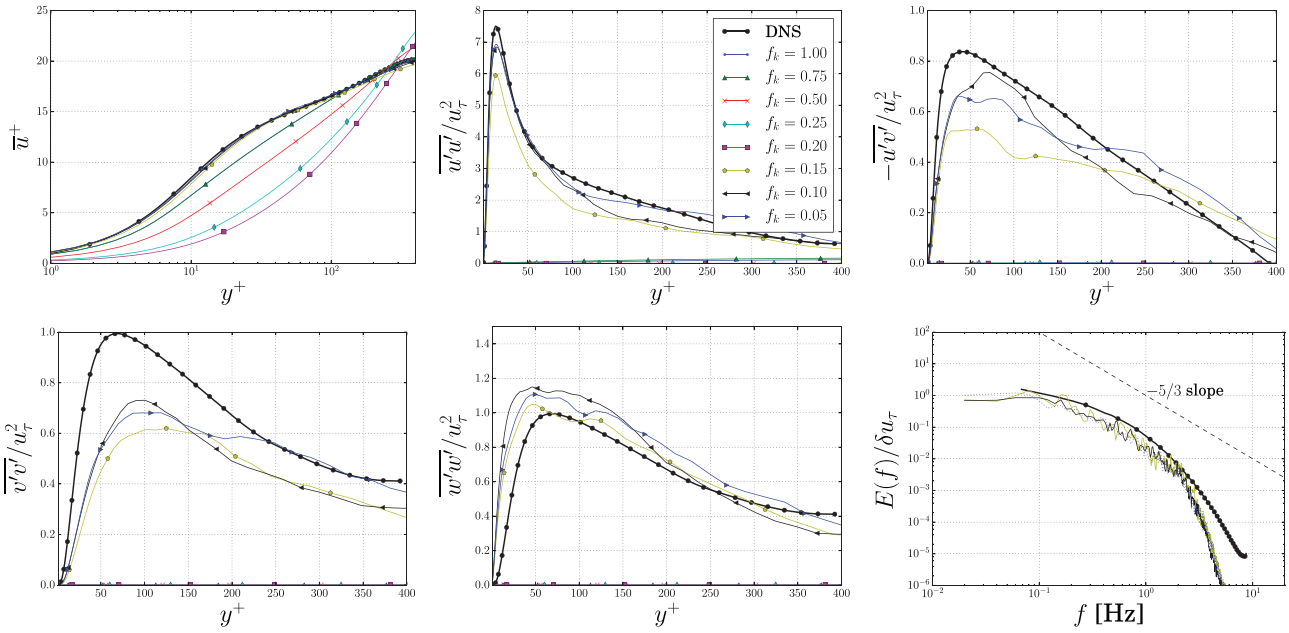

Fig. 12. Normalised mean velocity and Reynolds stress profiles and turbulence kinetic energy spectra using PANS and DNS [28]. From left to right, and top to bottom $\overline{u}^+$, Re_{uu}, Re_{uv}, Re_{vv}, Re_{ww} and $E_{u,y^+\approx 20}(f)$.

5.3. PANS

The PANS model is applied with $f_k = 0.75$, 0.50, 0.25, 0.20, 0.15, 0.10 and 0.05. Fig. 12 clearly shows the effect of reducing the f_k parameter on the mean velocity profile: $f_k = 1.00$ yields a RANS result as expected, while when moving from $f_k = 0.75$ to 0.20 the modelled turbulence kinetic energy is reduced and more turbulence kinetic energy should be resolved. However, by reducing f_k the flow profile becomes more laminar. Rather than resolving turbulence the velocity perturbations are damped and the flow remains laminar. The highest f_k values still have a reasonable match with the DNS, since these yield mostly turbulent RANS solutions. Below $f_k = 0.20$ the fluctuations are not damped and a fully turbulent flow develops. The results for $f_k = 0.15$, 0.10 and 0.05 match the DNS data velocity almost perfectly. The same behaviour occurs if PANS is applied to a fully developed turbulent flow (for instance obtained from a LES computation); for higher f_k values the fluctuations are damped after between five and seven flow-through times. The normalised Reynolds stress profiles and turbulence kinetic energy spectrum yield additional insight into this behaviour. It is clear that for computations with f_k in the range $0.75 - 0.20$ a laminar solution is obtained; the Reynolds stress tensor components equal zero. The Reynolds stress profiles and turbulence kinetic energy spectra $f_k = 0.15$, 0.10 and 0.05 are comparable and obtain the proper trends and order of magnitude. Interestingly, the peaks for $f_k = 0.10$ are higher than for $f_k = 0.15$ and 0.05. This is an indication of the need for finer grids and iterative convergence criteria for lower f_k values. For both $f_k = 0.10$ and 0.05 the match is better than for explicit LES, which is related to the increased turbulence resolution.

The turbulent structures in the flow are visualised in Fig. 13 for the lower f_k values. There is little difference between the different simulations. It appears that the results for cases with low f_k are identical to ILES. This is not true when looking at the eddy-viscosity, however. The maximum eddy-viscosity ratio, ν_t/ν, in the field for $f_k = 0.15$ has a magnitude of $\mathcal{O}(10^2)$, whereas for $f_k = 0.05$ this is $\mathcal{O}(10)$, and for ILES it is zero by definition. For comparison, for a turbulent RANS solution $\nu_t/\nu = \mathcal{O}(10^5)$. It is clear that the magnitude of eddy-viscosity has little effect on the results, provided that f_k is below the threshold to allow a turbulent flow.

The observed strong dependence on f_k, resulting in distinct laminar and turbulent flow regimes, is related to the physics of the problem. In a wall-bounded turbulent flow, such as a turbulent channel or flat plate, the small scales near the wall move away from the wall, and merge into increasingly larger scales away from the wall. The large scales then break up into small scales and are dissipated. This process is known as energy backscatter, or the inverse energy cascade [33]. A turbulent flow only develops if the filter length is smaller than the length scales of the small scales, otherwise the mechanism responsible for creating a fully turbulent flow is filtered out. This can occur on a coarse grid for all methods, or, in the case of PANS, when using a large f_k value. This hypothesis is confirmed by the guideline that for SRS the effective computational Reynolds number,

$$Re_e = \frac{U\delta}{\nu + \nu_{modelled}} = \frac{U\delta}{\nu + f_k^2\nu_t}, \tag{39}$$

must exceed the critical transition Reynolds number needed for the onset of instability, Re_c [72]. For a turbulent channel flow, this

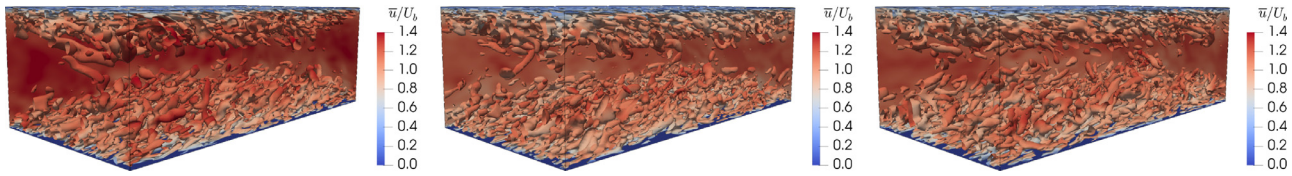

Fig. 13. PANS instantaneous turbulent flow fields ($Q = 0.3$), coloured by $u^* = u/U_b$. From left to right $f_k = 0.15$, 0.10 and 0.05.

guideline is satisfied for the cases with $f_k < 0.20$ ($Re_c \approx 2300$, obtained from experiments [73]). To enable turbulent results for f_k values in the range $0.20 - 1.00$ a synthetic turbulence generator is needed, which not only feeds the small scales, but also feeds energy directly into the larger scales to allow a turbulence cascade to develop. Note that the synthetic turbulence is inserted across the height of the channel, in contrast to the physics where turbulence develops parallel to the walls.

6. Comparison of turbulence approaches with synthetic turbulence generator

The second set of results is obtained by applying the synthetic turbulence generator described in Section 2.5. The turbulent fluctuations are added to the mean turbulent velocity profile, which is prescribed at the inlet. The domain is initialised with the mean turbulent flow profile, while the turbulence generator is located just behind the inlet. The body force terms are added over $L_{tg} = 0.1\delta$ which corresponds to two cells in the streamwise direction. In this case periodic boundary conditions are only applied in the spanwise direction. Based on the TST (see Section 4.2), temporal averaging of the results is performed over 7 flow-through times, after removing two flow-through times. The resulting statistical uncertainty for the mean streamwise velocity is below 3%, and for the Reynolds stress components below 12%. The mean velocity and Reynolds stress profiles prescribed are taken from the DNS reference data. The prescribed integral length scales are anisotropic but a homogeneous approximation is made based on the length scales given by Kim et al. [39]; in the streamwise direction the length scale is taken as 0.9δ, in the spanwise and wall perpendicular direction as 0.045δ. It is noted that, due to this assumption, the prescribed length scales at the wall are too large.

The application of a turbulence generator affects the iterative convergence; the L_2 and L_∞ norms are shown in Table 2. The ratio L_∞/L_2 is $\mathcal{O}(10^1)$ for synthetic cases compared to $\mathcal{O}(10^2)$ for recycling results, indicating that the residuals stagnate in a considerable part of the domain. Fig. 15 shows that this occurs in the cells close to the location at which the body force terms are applied, due to the local, explicit, addition of these terms, which also vary per time step. The close proximity of the turbulence generator to the inflow (where velocity is prescribed) also contributes to this situation.

It is observed that a streamwise development length is needed to allow the added perturbations to develop into a turbulent flow profile, and obtain a reasonable match with the input values. With the current implementation of the turbulence generator, after 6δ the results for $\overline{u}$ and Re_{uu} are self similar, as shown in Fig. 14. At this location, Re_{uv} is still underpredicted, Re_{uv} keeps developing until approximately 10δ. This is comparable to Kim et al. [39] and Xie and Castro [36], who both give a required development length of 10δ. The results shown in the remainder of this section are obtained at a location 6δ behind the turbulence generator.

Table 2
Average residual norms for recycling and synthetic cases.

Equation	Recycling		Synthetic	
	L_∞	L_2	L_∞	L_2
Momentum:	10^{-5}	10^{-6}	10^{-2}	10^{-4}
Pressure:	10^{-6}	10^{-7}	10^{-4}	10^{-6}
Turbulence:	10^{-6}	10^{-7}	10^{-7}	10^{-9}

In order to compare the results obtained from recycling and synthetic computations, Fig. 16 shows the resolved turbulence intensity versus the channel height for all models. As shown in Section 5, for the recycling cases, the LES models show the best match with the reference data, together with the PANS results with $f_k < 0.2$. The synthetic results however, are similar for all models. With the exception of PANS, I is overpredicted at the centre of the domain. Both DDES and PANS with higher f_k show an underprediction of I at the wall. The PANS results show an increase in I with decreasing f_k, as might be expected. Nevertheless the results show that the application of a synthetic turbulence generator can prevent the occurrence of laminar flow for cases where the critical transition Reynolds number exceeds the effective computational Reynolds number (as is the case for $f_k \geq 0.20$, see Section 5.3).

6.1. LES

Fig. 17 shows the results obtained using different LES models. As expected the shape of the mean velocity profiles matches the DNS data well, however an underprediction occurs across the channel height. For Re_{uu}, ILES and WALE have the correct peak value, with the other models showing the correct shape but a lower peak. In contrast to the recycling results (Fig. 7), where all models underpredicted Re_{uv} and Re_{vv}, the results lie on or above the DNS data for all models except the Lilly model. This model *does* accurately predict Re_{ww} however, which is overpredicted by the other models. For the turbulence kinetic energy spectrum, the ILES and WALE model contain the most energy, while the spectrum for the Lilly model shows less energy than for the recycling cases. The underprediction by the Lilly model is similar to that already shown in Fig. 7 and is again related to the application of the larger 'test' filter, which filters out synthetic turbulence.

6.2. Hybrid models

The results obtained using different Hybrid models are shown in Fig. 18. For the mean velocity, the same underprediction occurs as for the LES models. The results for the DDES model are improved with respect to recycling cases (Fig. 9): the magnitude is still significantly underpredicted but the distribution of the Reynolds stress components is closer to the DNS data, and there is more energy in the spectrum. For the IDDES model, the Reynolds stresses are also higher compared to the recycling results. The peak of Re_{uu}, Re_{uv} and Re_{vv} is better captured, but Re_{ww} is overpredicted. The XLES results are similar to the IDDES results, with the exception of an underprediction of Re_{uu} near the wall which was also observed for recycling cases. The energy in the turbulence kinetic energy spectrum is lower for XLES than for IDDES, exhibiting a magnitude similar to DDES. For all models Re_{uv} is underpredicted at the centre, which was not the case for the recycling results.

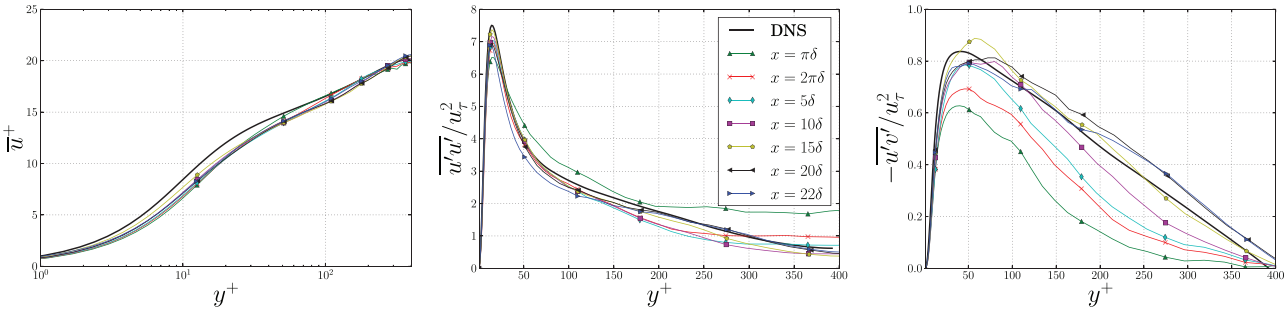

Fig. 14. Normalised mean velocity and Reynolds stress profiles at different downstream locations using PANS with $f_k = 0.05$ and a turbulence generator. From left to right, $\overline{u}^+$, Re_{uu} and Re_{uv}.

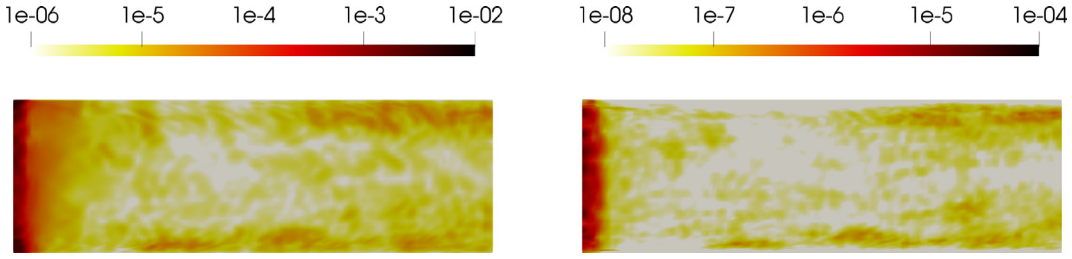

Fig. 15. Velocity (left) and pressure (right) residuals in the domain for a PANS computation with turbulence generator ($f_k = 0.05$). The turbulence generator is located at the left of the images.

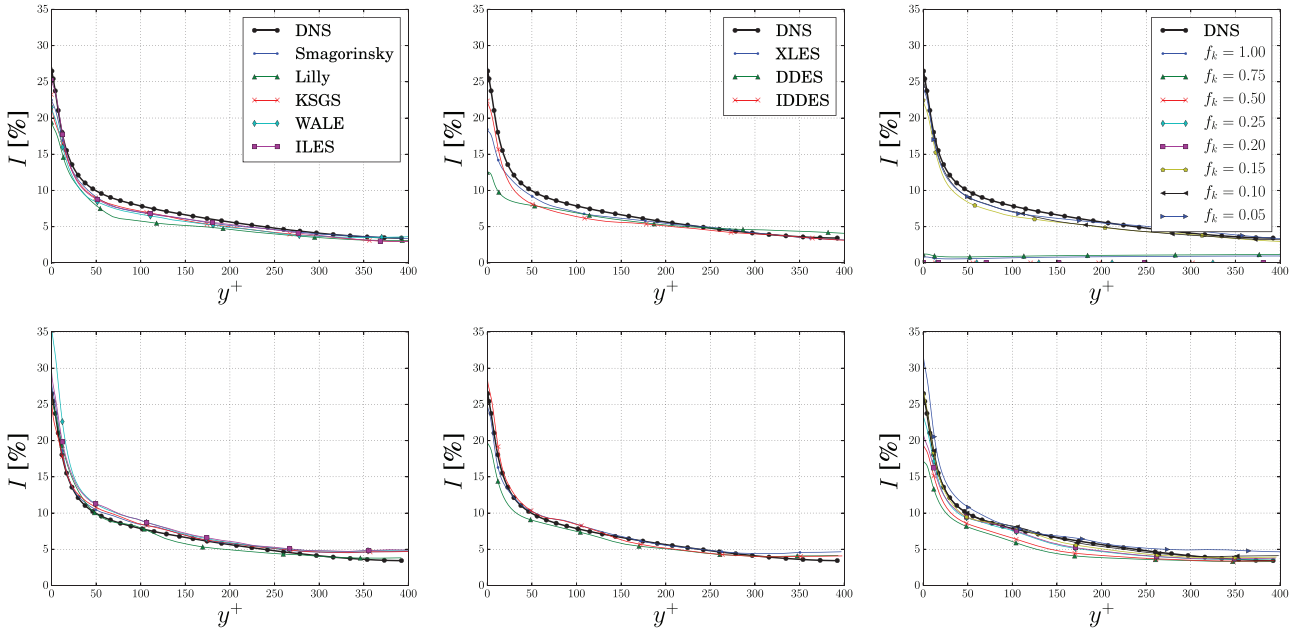

(a) LES (b) Hybrid (c) PANS

Fig. 16. Resolved turbulence intensity ($I = 1/3\sqrt{\overline{u_i'u_i'}}/\overline{u}$) for recycling (top row) and turbulence generator (bottom row) for LES, Hybrid and PANS models. Results obtained at $x = 2\delta$ and averaged in transverse direction.

6.3. PANS

Fig. 19 shows the results obtained using PANS with different f_k values. As seen for the other synthetic results, the mean velocity is underpredicted. For all components of the Reynolds stresses a similar behaviour is observed; with decreasing f_k the results converge towards the DNS data with decreasing f_k. Re_{uu} is overpredicted at the centre with $f_k = 0.05$. The same occurs for Re_{ww} when $f_k \leq 0.25$, but then across the full channel height. The increase in fluctuations with decreasing f_k can be related to the results obtained without turbulence generator: the addition of synthetic turbulence leads to a turbulent profile, yet computations with higher f_k values add dissipation, thereby damping the resolved turbulence. Consequently, the resolved Reynolds stresses decrease in magnitude. This is most visible in the turbulence kinetic energy spectra, where the cut-off frequency increases with decreasing f_k.

Fig. 20 visualises the turbulent structures from PANS, based on Q. The most important difference with the results presented in Section 5.3 (Fig. 13) is that for $f_k > 0.15$ turbulent structures now exist in the flow. However for these higher f_k values the

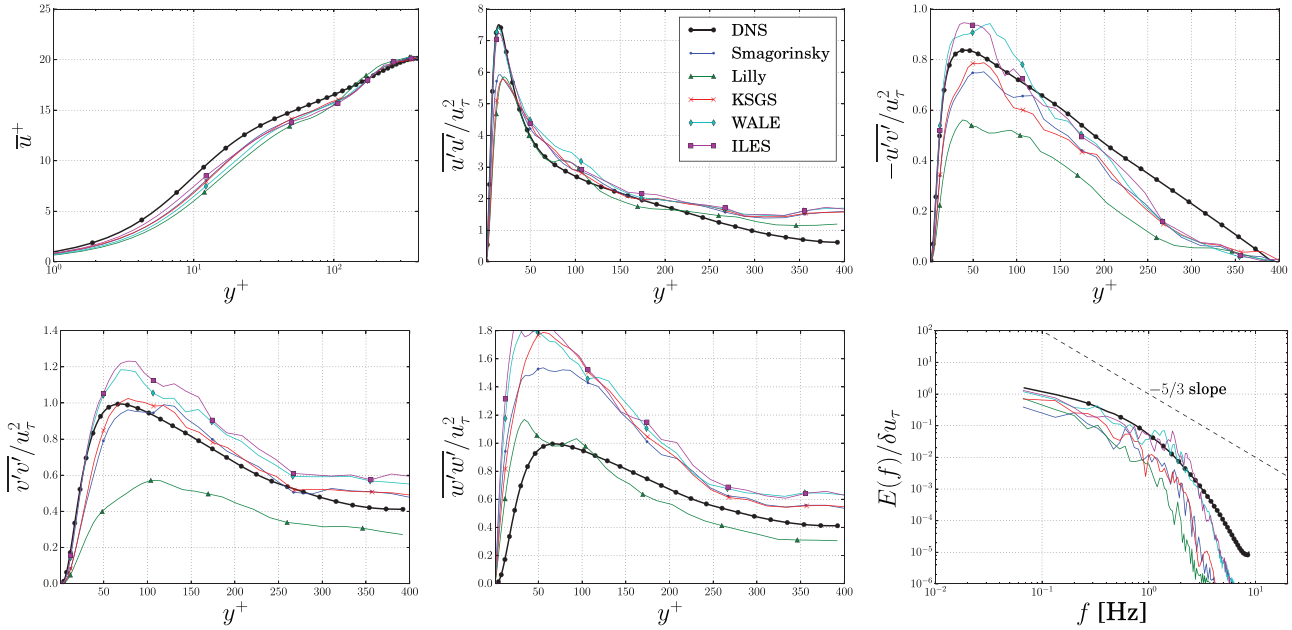

Fig. 17. Normalised mean velocity and Reynolds stress profiles and turbulence kinetic energy spectra using LES and a turbulence generator. From left to right, and top to bottom $\overline{u}^+$, Re_{uu}, Re_{uv}, Re_{vv}, Re_{ww} and $E_{u,y^+\approx 20}(f)$. Results obtained at $x = 2\delta$ and averaged in transverse direction.

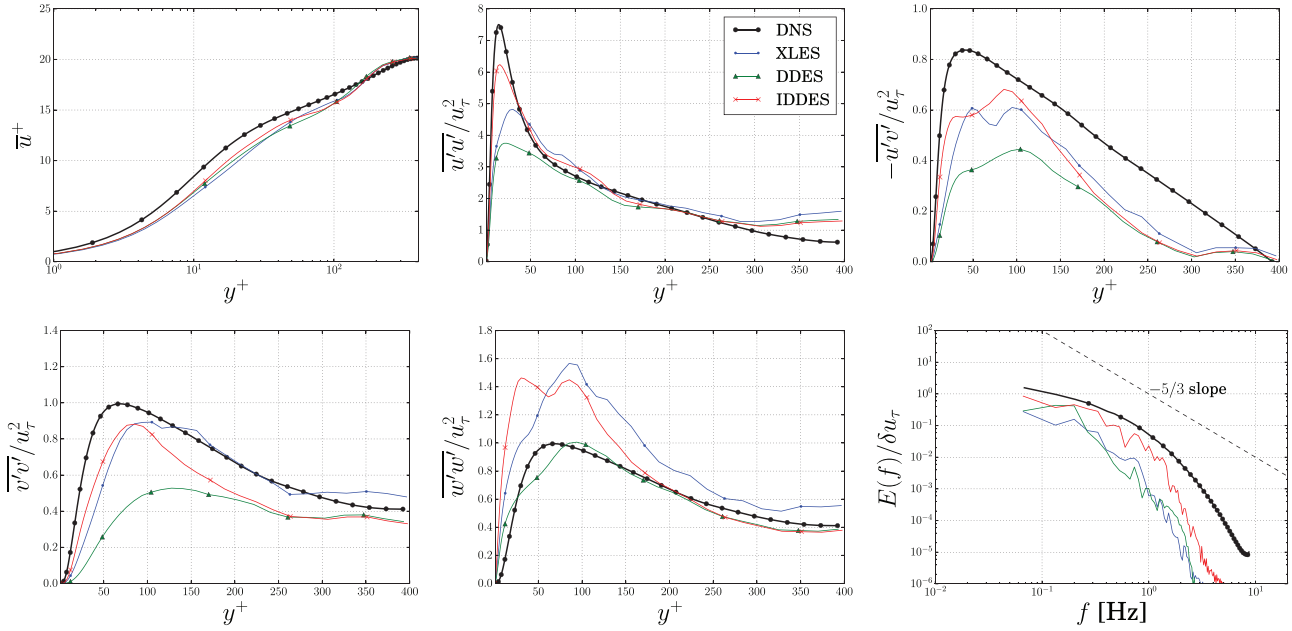

Fig. 18. Normalised mean velocity and Reynolds stress profiles and turbulence kinetic energy spectra using Hybrid models and a turbulence generator. From left to right, and top to bottom $\overline{u}^+$, Re_{uu}, Re_{uv}, Re_{vv}, Re_{ww} and $E_{u,y^+\approx 20}(f)$. Results obtained at $x = 2\delta$ and averaged in transverse direction.

fluctuations are filtered by the model as they propagate downstream of the turbulence generator, as can be most clearly seen near the walls. The images are similar to the recycling results for the lower f_k values ($f_k \leq 0.15$), however close to the turbulence generator more structures can be seen in the centre of the channel.

7. Discussion

In this work turbulence is generated both using streamwise periodic boundary conditions and a pressure gradient, i.e. as precursor (Section 5), and using a synthetic turbulence generator (Section 6). For industrial CFD it is shown that, independent of the selected turbulence simulation approach, the synthetic method can produce a turbulent inflow at significantly lower computational cost. Only two flow-through times from generator to object of interest have to be computed before statistics can be collected based on the TST, in contrast to the precursor computations for which 11 flow-through times were required (Section 4.2). The ability to more easily tune the method to obtain the desired Reynolds stresses and length scales is also attractive for industrial applications for which these quantities may already be known. Finally, it is noted that for a range of industrial test cases, such as foils, wings or propellers, only homogeneous inflow turbulence is required. For such cases, the advantages of a synthetic generator clearly show; no flow recycling is required, and the grid only needs to be refined around the object of interest and upstream.

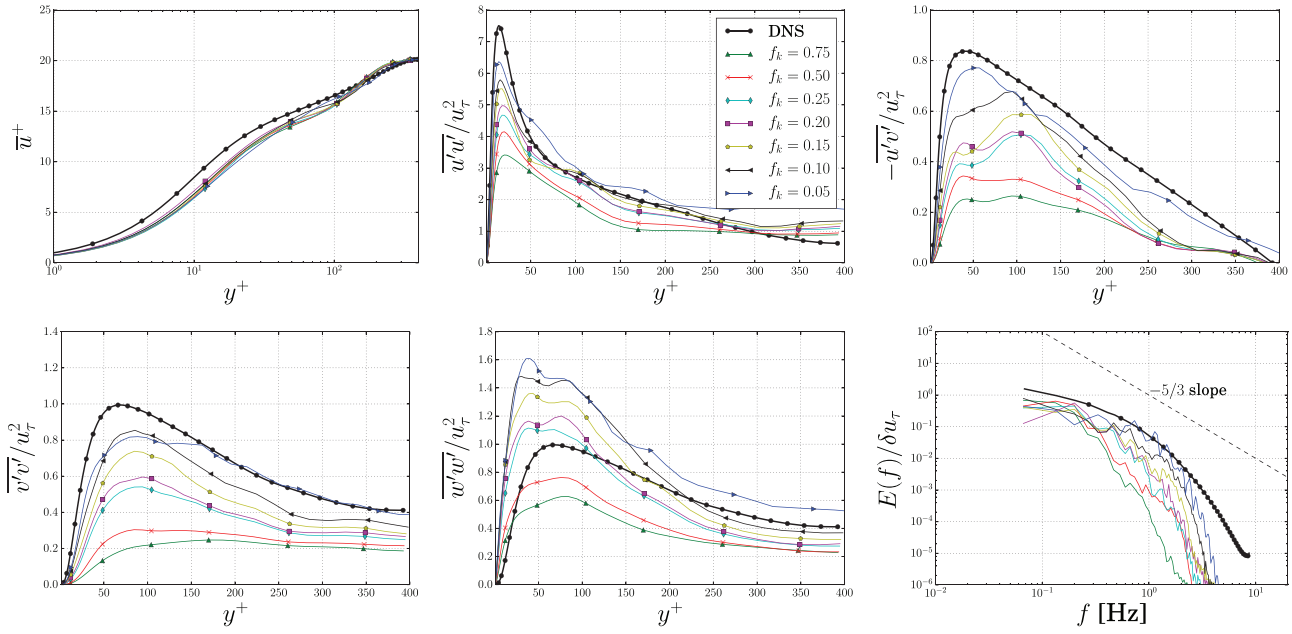

Fig. 19. Normalised mean velocity and Reynolds stress profiles and turbulence kinetic energy spectra using PANS and a turbulence generator. From left to right, and top to bottom $\overline{u}^+$, Re_{uu}, Re_{uv}, Re_{vv}, Re_{ww} and $E_{u,y^+\approx 20}(f)$. Results obtained at $x = 2\delta$ and averaged in transverse direction.

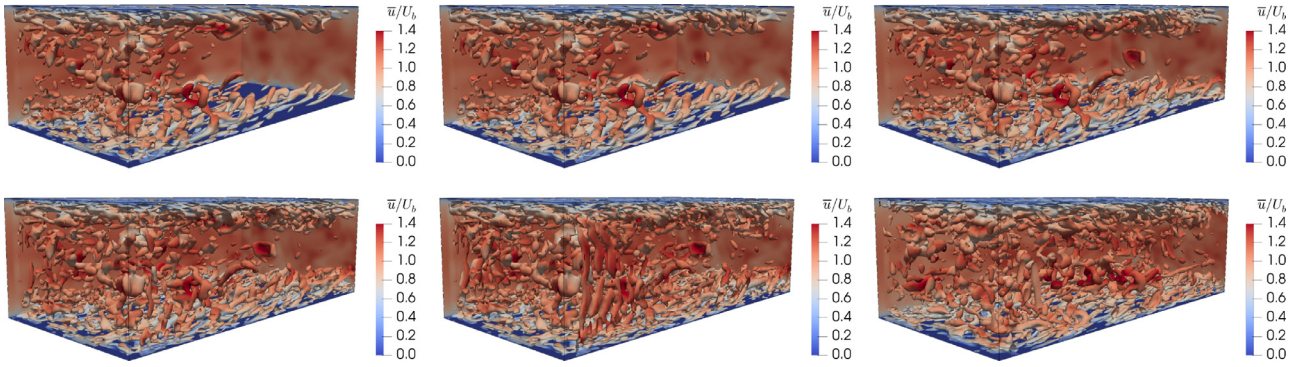

Fig. 20. PANS with turbulence generator, instantaneous turbulent flow fields ($Q = 0.3$), coloured by $u^* = u/U_b$. From left to right, and top to bottom $f_k = 0.75$, 0.50, 0.25, 0.15, 0.10 and 0.05. Turbulence generator is located at the left of the images.

A cause of concern is the possible introduction of additional numerical errors by the synthetic turbulence generator. The main error sources are: not satisfying mass conservation, interpolation, and iterative errors. In the present study, the pressure fluctuations introduced by the turbulence generator were observed to be of the same order of magnitude as the pressure fluctuations in recycling cases (results not shown in this paper), indicating that the introduced turbulence satisfies mass continuity. Interpolation errors occur between the grid on which random numbers are generated, and the CFD grid. However, due to the finer density of the CFD grid compared to the density of the random number grid (which is a consequence of the desired length scales), this error is small. It is also important to keep in mind that the velocity fluctuations themselves are not interpolated to the CFD grid, but rather the body-force terms which perturb the flow, thereby decreasing the sensitivity to the interpolation. Note that a precursor turbulence generator may also not be entirely free from interpolation errors, depending on the two grids used.

The application of the synthetic turbulence generator does significantly worsen the convergence behaviour when compared to recycling cases (Sections 4.1 and 6). The solver does not converge in the cells near the generator where the body-force terms are added. If the generator is located further from the inflow, the residuals can be reduced by about one order of magnitude, but stagnation still occurs (results not shown in this paper). However the residuals show that the lack of convergence is a local effect (Fig. 15), and by definition the object of interest must be located far from the turbulence generator to allow for a sufficient development length [11]. It is expected that the turbulence generator has little effect on the iterative error at the object of interest, and therefore these cells could be excluded from the reported maximum residuals in the domain.

While potentially introducing numerical errors, it is clear that the turbulence generator significantly reduces modelling errors by improving the similarity between computations and experimental setups. This is beneficial not only for SRS techniques such as LES and PANS which yield unphysical laminar and/or separating flows without proper inflow conditions [10], but also for Hybrid models where the problems tend to be more concealed. Finally, while both precursor and synthetic turbulence generation methods are independent of the turbulence simulation approach, it should be emphasised that recycling in combination with PANS using insufficiently low f_k values does not lead to a turbulent flow (see Fig. 12). To enable the use of this model with these settings, the synthetic method is required.

8. Conclusions

A turbulent channel flow at $Re_\tau = 395$ is simulated using two approaches for generating inflow turbulence. The interaction of these methods with several SRS models is investigated, and the results are compared to DNS reference data. For recycling cases the numerical errors are also evaluated. Based on the normalised residuals it is shown that the iterative error was negligible. The statistical uncertainty based on 45 flow-through times was below 2% for the mean values, and below 10% for the Reynolds stresses. The grids employed satisfy LES recommendations from the open literature. It is shown that the discretisation error due to the grid is negligible, the discretisation of the convective terms in the momentum equations having a larger effect. Best results are obtained with a second-order accurate CD scheme.

For LES, the magnitude of the turbulent fluctuations depends on the sub-filter modelling. Due to the fine grid resolution however, the difference between the LES models was found to be small. The Lilly and WALE model predict larger turbulent structures than the other models. On coarser grids explicit LES predicts the Reynolds stresses more accurately than ILES. In contrast, Hybrid models, which are often favoured in industrial applications, show less satisfactory results. Both XLES and IDDES have a reasonable match; the velocity profiles are close to the reference data, and the Reynolds stresses, although underpredicted in magnitude, show the correct shape. Due to the formulation of the IDDES model, the Reynolds stresses are especially underpredicted close to the wall. While the formulation of the DDES model should lead to a full RANS behaviour, in the centre of the domain a LES behaviour was observed. Finally the application of PANS showed that there is a case-dependent threshold which separates two solution regimes: $0.20 \leq f_k < 1.0$ yields a laminar solution regardless of the initialisation of the flow, while if $f_k < 0.20$ a turbulent flow can develop. The results are then very similar to ILES, since due to the low f_k the RANS formulation in the PANS model has little effect. This finding is supported by the visualised turbulent structures and an investigation into the effect of grid coarsening, where PANS with $f_k = 0.10$ and ILES follow the same trend.

The application of a synthetic turbulence generator shows that results comparable to recycling computations can be obtained at reduced computational cost. In this case, the PANS model with higher f_k values also results in a turbulent flow. Ease of usage and tuning makes the use of the synthetic turbulence generator promising in order to obtain a representative inflow for industrial CFD applications. Further work includes improving the iterative convergence behaviour and the application of the method to industrial test cases.

Declaration of Competing Interest

The authors declare that they have no known competing financial interests or personal relationships that could have appeared to influence the work reported in this paper.

CRediT authorship contribution statement

M. Klapwijk: Conceptualization, Methodology, Software, Investigation, Formal analysis, Visualization, Writing - original draft. **T. Lloyd:** Conceptualization, Writing - review & editing, Supervision. **G. Vaz:** Conceptualization, Writing - review & editing, Supervision. **T. van Terwisga:** Funding acquisition, Supervision.

Acknowledgements

This research was financially supported by the Dutch Research Council (NWO), as part of the NOISOURCE project (ALWTW.2016.008), and by the Dutch Ministry of Economic Affairs. The work was carried out on the Dutch national e-infrastructure, with the support of SURF Cooperative, on the *Reynolds* (TU Delft) and *Marclus3* (MARIN) clusters.

Appendix A

A1. $k-\omega$ SST2003

The auxiliary functions are

$$F_1 = \tanh\left(\min\left(\max\left(\frac{\sqrt{k}}{\beta^* \omega d}, \frac{500\nu}{d^2\omega}\right), \frac{4\rho\sigma_{\omega_2} k}{d^2 \max\left(\frac{2\rho\sigma_{\omega_2}}{\omega}\frac{\partial k}{\partial x_j}\frac{\partial \omega}{\partial x_j}, 10^{-10}\right)}\right)^4\right), \tag{40}$$

$$F_2 = \tanh\left(\max\left(\frac{2\sqrt{k}}{\beta^* \omega d}, \frac{500\nu}{d^2\omega}\right)^2\right), \tag{41}$$

in which d is the wall distance. The coefficients are defined in Table 3, and can be computed using

$$\Phi = \Phi_1 F_1 + \Phi_2 (1.0 - F_1). \tag{42}$$

A2. DDES

The coefficients for the $k-\omega$ DDES model are presented in Table 4. The maximum cell length is given by

$$\Delta = \max(\Delta_x, \Delta_y, \Delta_z) \tag{43}$$

and the coefficients can be obtained from

$$C_{DDES} = F_1 C_{DDES_1} + (1 - F_1) C_{DDES_2}. \tag{44}$$

f_d is the empirical shielding function to prevent grid induced separation in the DDES formulation [13]

$$f_d = 1 - \tanh\left[\left(C_{d_1}\frac{\nu_t + \nu}{\kappa^2 d^2 \sqrt{0.5\left(\langle S\rangle^2 + \langle\Omega\rangle^2\right)}}\right)^{C_{d_2}}\right]. \tag{45}$$

A3. IDDES

The coefficients for the $k-\omega$ IDDES model are presented in Table 5. The length scale and SRS length scales are defined as

$$l_t = \tilde{f}_d l_t^{RANS} + \left(1 - \tilde{f}_d\right) l_t^{SRS}, \tag{46}$$

$$l_t^{SRS} = C_{IDDES} \min(C_w \max(d, \Delta), \Delta), \tag{47}$$

$$C_{IDDES} = F_1 C_{IDDES} + (1 - F_1) C_{IDDES} \tag{48}$$

and depend on an empirical delay function

$$\tilde{f}_d = \max(1 - f_{dt}, f_b). \tag{49}$$

The shielding functions are

$$f_{dt} = 1 - \tanh\left[\left(C_{dt_1}\frac{\nu_t}{\kappa^2 d^2 \sqrt{0.5\left(\langle S\rangle^2 + \langle\Omega\rangle^2\right)}}\right)^{C_{dt_2}}\right], \tag{50}$$

$$f_b = \min\left(2.0\exp\left(-9.0\left(0.25 - \frac{d}{\Delta}\right)^2\right), 1.0\right). \tag{51}$$

Table 3
Coefficients of the $k-\omega$ SST2003 turbulence model.

α_1	α_2	a_1	β_1	β_2	β^*	σ_{k_1}	σ_{k_2}	σ_{ω_1}	σ_{ω_2}
5/9	0.440	0.310	0.075	0.0828	0.090	0.850	1.000	0.500	0.856

Table 4
Coefficients of the $k-\omega$ DDES turbulence model.

β^*	C_{d_1}	C_{d_2}	C_{DDES_1}	C_{DDES_2}	κ
0.09	20	3	0.78	0.61	0.41

Table 5
Coefficients of the $k-\omega$ IDDES turbulence model.

β^*	C_{d_1}	C_{d_2}	C_w	C_{IDDES_1}	C_{IDDES_2}	κ
0.09	20	3	0.15	0.78	0.61	0.41

Table 6
Coefficients of the XLES turbulence model.

C_1	β_k	β_ω	σ_k	σ_ω	σ_d	α_ω
0.05	0.09	0.075	2/3	0.5	0.5	0.55

A4. XLES

The composite length scale in the XLES model is defined as

$$\tilde{l} = \min(l, C_1\Delta), \tag{52}$$

such that

$$\nu_t = \tilde{l}\sqrt{k} \qquad \text{and} \qquad \epsilon = \beta_k \frac{k^{\frac{3}{2}}}{\tilde{l}}. \tag{53}$$

The grid size Δ is taken as

$$\Delta = \max(\Delta_x, \Delta_y, \Delta_z). \tag{54}$$

C_2 and α_ω are defined as

$$C_2 = \frac{\beta_k}{C_1} \qquad \text{and} \qquad \alpha_\omega = \frac{\beta_\omega}{\beta_k} - \frac{\sigma_\omega \kappa^2}{\sqrt{\beta_k}}. \tag{55}$$

The other constants are given in Table 6.

A5. PANS

The auxiliary functions, F_1 and F_2, are

$$F_1 = \tanh\left(\min\left(\max\left(\frac{\sqrt{k}}{0.09\omega d}, \frac{500\nu}{d^2\omega}\right), \frac{4\rho\sigma_{\omega_2}k}{d^2 \max\left(\frac{2\rho\sigma_{\omega_2}}{\omega}\frac{\partial k}{\partial x_j}\frac{\partial \omega}{\partial x_j}, 10^{-10}\right)}\right)^4\right) \tag{56}$$

and

$$F_2 = \tanh\left(\max\left(\frac{2\sqrt{k}}{0.09\omega d}, \frac{500\nu}{d^2\omega}\right)^2\right) \tag{57}$$

with the constants given in Table 3. Details on the implementation can be found in Pereira et al. [50,74].

References

[1] Rezaeiravesh S, Liefvendahl M, Fureby C. On grid resolution requirements for LES of wall-bounded flows. In: ECCOMAS Congress 2016, June 5–10, Crete, Greece. European Community on Computional Methods in Applied Sciences (ECCOMAS); 2016. p. 7454–65.

[2] Girimaji S, Abdol-Hamid K. Partially averaged Navier-Stokes model for turbulence: implementation and validation. In: 43rd AIAA Aerospace Sciences Meeting and Exhibit; 2005. p. 502.

[3] Spalart P. Comments on the feasibility of LES for wings, and on a hybrid RANS/LES approach. In: Proceedings of first AFOSR international conference on DNS/LES. Greyden Press; 1997.

[4] Ghosal S, Moin P. The basic equations for the large eddy simulation of turbulent flows in complex geometry. J Comput Phys 1995;118(1):24–37.

[5] Mockett C, Haase W, Thiele F. Go4Hybrid: a European initiative for improved Hybrid RANS-LES modelling. In: Progress in Hybrid RANS-LES Modelling. Springer; 2015. p. 299–303.

[6] Luo D, Yan C, Liu H, Zhao R. Comparative assessment of PANS and DES for simulation of flow past a circular cylinder. J Wind Eng Ind Aerodyn 2014;134:65–77.

[7] Zhang J, Minelli G, Rao A, Basara B, Bensow R, Krajnović S. Comparison of PANS and LES of the flow past a generic ship. Ocean Eng 2018;165:221–36.

[8] Jarrin N, Benhamadouche S, Laurence D, Prosser R. A synthetic-eddy-method for generating inflow conditions for large-eddy simulations. Int J Heat Fluid Flow 2006;27(4):585–93.

[9] Klein M, Sadiki A, Janicka J. A digital filter based generation of inflow data for spatially developing direct numerical or large eddy simulations. J Comput Phys 2003;186(2):652–65.

[10] Lund T, Wu X, Squires K. Generation of turbulent inflow data for spatially-developing boundary layer simulations. J Comput Phys 1998;140(2):233–58.

[11] Tabor G, Baba-Ahmadi M. Inlet conditions for large eddy simulation: a review. Comput Fluid 2010;39(4):553–67.

[12] Luo D. Numerical simulation of turbulent flow over a backward facing step using partially averaged Navier-Stokes method. J Mech Sci Technol 2019;33(5):2137–48.

[13] Spalart P, Deck S, Shur M, Squires K, Strelets M, Travin A. A new version of detached-eddy simulation, resistant to ambiguous grid densities. Theor Comput Fluid Dyn 2006;20(3):181–95.

[14] Shur M, Spalart P, Strelets M, Travin A. A hybrid RANS-LES approach with delayed-DES and wall-modelled LES capabilities. Int J Heat Fluid Flow 2008;29(6):1638–49.

[15] Kok J, Dol H, Oskam B, van der Ven H. Extra-large eddy simulation of massively separated flows. AIAA paper 2004;264.

[16] Smagorinsky J. General circulation experiments with the primitive equations: I. The basic experiment. Mon Weather Rev 1963;91(3):99–164.

[17] Germano M, Piomelli U, Moin P, Cabot W. A dynamic subgrid-scale eddy viscosity model. Phys Fluid A 1991;3(7):1760–5.

[18] Lilly D. A proposed modification of the Germano subgrid-scale closure method. Phys. Fluid. A 1992;4(3):633–5.

[19] Nicoud F, Ducros F. Subgrid-scale stress modelling based on the square of the velocity gradient tensor. Flow, Turbul Combust 1999;62(3):183–200.

[20] Davidson L. Large eddy simulation: A dynamic one-equation subgrid model for three-dimensional recirculating flow. In: 11th Int. Symp. on Turbulent Shear Flow, 3; 1997. p. 261–6.

[21] Schumann U. Subgrid scale model for finite difference simulations of turbulent flows in plane channels and annuli. J Comput Phys 1975;18(4):376–404.

[22] Moin P, Kim J. Numerical investigation of turbulent channel flow. J Fluid Mech 1982;118:341–77.

[23] Mason P, Callen N. On the magnitude of the subgrid-scale eddy coefficient in large-eddy simulations of turbulent channel flow. J Fluid Mech 1986;162:439–62.

[24] Kim J, Moin P, Moser R. Turbulence statistics in fully developed channel flow at low Reynolds number. J Fluid Mech 1987;177:133–66.

[25] Piomelli U, Moin P, Ferziger J. Model consistency in large eddy simulation of turbulent channel flows. Phys Fluid 1988;31(7):1884–91.

[26] Wang Q, Squires K. Large eddy simulation of particle-laden turbulent channel flow. Phys Fluid 1996;8(5):1207–23.

[27] Wang Q, Squires K. Large eddy simulation of particle deposition in a vertical turbulent channel flow. Int J Multiphase Flow 1996;22(4):667–83.

[28] Moser R, Kim J, Mansour N. Direct numerical simulation of turbulent channel flow up to $Re_\tau = 590$. Phys Fluid 1999;11(4):943–5.

[29] Hughes T, Oberai A, Mazzei L. Large eddy simulation of turbulent channel flows by the variational multiscale method. Phys Fluid 2001;13(6):1784–99.

[30] Scotti A, Piomelli U. Numerical simulation of pulsating turbulent channel flow. Phys Fluid 2001;13(5):1367–84.

[31] de Villiers E. The potential of Large Eddy Simulation for the modelling of wall bounded flows. University of London; 2007.

[32] Nikitin N, Nicoud F, Wasistho B, Squires K, Spalart P. An approach to wall modeling in large-eddy simulations. Phys Fluid 2000;12(7):1629–32.

[33] Cimarelli A, De Angelis E. The physics of energy transfer toward improved subgrid-scale models. Phys Fluid 2014;26(5):055103.

[34] Mukha T., Liefvendahl M.. Large-eddy simulation of turbulent channel flow. 2015. https://pdfs.semanticscholar.org/bb2f/67c2296c6ba6545c59e870562348347f2825.pdf.

[35] Razi P. Partially-averaged Navier-Stokes (PANS) method for turbulence simulations: near-wall modeling and smooth-surface separation computations. Texas A & M University; 2015.

[36] Xie Z-T, Castro I. Efficient generation of inflow conditions for large eddy simulation of street-scale flows. Flow Turbul Combust 2008;81(3):449–70.
[37] Gilling L, Sørensen N, Davidson L. Detached eddy simulations of an airfoil in turbulent inflow. In: 47th AIAA Aerospace Sciences Meeting Including The New Horizons Forum and Aerospace Exposition; 2009. p. 270.
[38] Jarrin N, Prosser R, Uribe J-C, Benhamadouche S, Laurence D. Reconstruction of turbulent fluctuations for hybrid RANS/LES simulations using a synthetic-eddy method. Int J Heat Fluid Flow 2009;30(3):435–42.
[39] Kim Y, Castro I, Xie Z. Divergence-free turbulence inflow conditions for large-eddy simulations with incompressible flow solvers. Comput Fluid 2013;84:56–68.
[40] Poletto R, Craft T, Revell A. A new divergence free synthetic eddy method for the reproduction of inlet flow conditions for LES. Flow Turbul Combust 2013;91(3):519–39.
[41] Bercin K, Xie Z-T, Turnock S. Exploration of digital-filter and forward-stepwise synthetic turbulence generators and an improvement for their skewness-kurtosis. Comput Fluid 2018;172:443–66.
[42] Breuer M. Effect of inflow turbulence on an airfoil flow with laminar separation bubble: an LES study. Flow Turbul Combust 2018:1–24.
[43] Kröger H, Kornev N. Generation of divergence free synthetic inflow turbulence with arbitrary anisotropy. Comput Fluid 2018;165:78–88.
[44] Patruno L, Ricci M. A systematic approach to the generation of synthetic turbulence using spectral methods. Comput Methods Appl Mech Eng 2018;340:881–904.
[45] Xie B, Gao F, Boudet J, Shao L, Lu L. Improved vortex method for large-eddy simulation inflow generation. Comput Fluid 2018;168:87–100.
[46] Germano M. Turbulence: the filtering approach. J Fluid Mech 1992;238:325–36.
[47] Menter F, Kuntz M, Langtry R. Ten years of industrial experience with the SST turbulence model. Turbul Heat Mass Transf 2003;4(1):625–32.
[48] Gritskevich M, Garbaruk A, Schütze J, Menter F. Development of DDES and IDDES formulations for the k-ω shear stress transport model. Flow Turbul Combust 2012;88(3):431–49.
[49] Kok J. Resolving the dependence on freestream values for the $k-\omega$ turbulence model. AIAA J 2000;38(7):1292–5.
[50] Pereira F, Vaz G, Eça L, Girimaji S. Simulation of the flow around a circular clinder at Re=3900 with partially-averaged Navier-Stokes equations. Int J Heat Fluid Flow 2018;69:234–46.
[51] Reyes D, Cooper J, Girimaji S. Characterizing velocity fluctuations in partially resolved turbulence simulations. Phys Fluid 2014;26(8):085106.
[52] Klapwijk M, Lloyd T, Vaz G, van Terwisga T. PANS simulations: low versus high Reynolds number approach. In: VIII International Conference on Computational Methods in Marine Engineering (MARINE 2019), Gothenborg, Sweden; 2019.
[53] Klapwijk M, Lloyd T, Vaz G. On the accuracy of partially averaged Navier-Stokes resolution estimates. Int J Heat Fluid Flow 2019;80:108484.
[54] Nicoud F, Toda H, Cabrit O, Bose S, Lee J. Using singular values to build a subgrid-scale model for large eddy simulations. Phys Fluid 2011;23(8):085106.
[55] Grinstein F, Margolin L, Rider W. Implicit large eddy simulation: computing turbulent fluid dynamics. Cambridge university press; 2007.
[56] Georgiadis N, Rizzetta D, Fureby C. Large-eddy simulation: current capabilities, recommended practices, and future research. AIAA J 2010;48(8):1772–84.
[57] Schoppa W, Hussain F. Coherent structure dynamics in near-wall turbulence. Fluid Dyn Res 2000;26(2):119–39.
[58] Klapwijk M, Lloyd T, Vaz G, van Terwisga T. Channel flow at $Re_\tau = 395$: LES is more (turbulent than PANS). 21st Numerical Towing Tank Symposium (NuTTS'18), Cortona, Italy; 2018.
[59] Pope S. Turbulent flows. Cambridge University Press; 2000. ISBN 9780521598866.
[60] Vaz G, Jaouen F, Hoekstra M. Free-surface viscous flow computations: validation of URANS code FRESCO. In: ASME 2009 28th International Conference on Ocean, Offshore and Arctic Engineering. American Society of Mechanical Engineers; 2009. p. 425–37.
[61] Roache P. Fundamentals of verification and validation. hermosa publ.; 2009.
[62] Eça L, Vaz G, Hoekstra M. On the role of iterative errors in unsteady flow simulations. 21st Numerical Towing Tank Symposium (NuTTS'18), Cortona, Italy; 2018.
[63] Brouwer J, Tukker J, Van Rijsbergen M. Uncertainty analysis and stationarity test of finite length time series signals. In: The 4th International Conference on Advanced Model Measurement Technology for the Maritime Industry (AMT15), Istanbul, Turkey; 2015.
[64] Ries F, Nishad K, Dressler L, Janicka J, Sadiki A. Evaluating large eddy simulation results based on error analysis. Theor Comput Fluid Dyn 2018:1–20.
[65] Piomelli U, Balaras E. Wall-layer models for large-eddy simulations. Annu Rev Fluid Mech 2002;34(1):349–74.
[66] Basara B, Pavlovic Z, Krajnovic S. Effects of convection schemes on hybrid RANS-LES calculations. In: Symposium on Hybrid RANS-LES Methods. Springer; 2016. p. 145–55.
[67] Basara B, Krajnovic S, Girimaji S. PANS vs. LES for computations of the flow around a 3D bluff body. In: Proc. of ERCOFTAC 7th Int. Symp.-ETMM7, Lymassol, Cyprus, 2; 2008. p. 3.
[68] Ferziger J, Perić M, Street R. Computational methods for fluid dynamics. Springer International Publishing; 2019. ISBN 9783319996936.
[69] Meyers J, Sagaut P. Is plane-channel flow a friendly case for the testing of large-eddy simulation subgrid-scale models? Phys Fluid 2007;19(4):048105.
[70] Rozema W, Verstappen R, Veldman A, Kok J. Low-dissipation simulation methods and models for turbulent subsonic flow. Arch Comput Methods Eng 2018:1–32.
[71] Kamkar S, Jameson A, Wissink A, Sankaran V. Feature-driven cartesian adaptive mesh refinement in the helios code. 48th AIAA Aerospace Sciences Meeting Including the New Horizons Forum and Aerospace Exposition, AIAA, 171; 2010.
[72] Pereira F, Eça L, Vaz G, Girimaji S. Challenges in scale-resolving simulations of turbulent wake flows with coherent structures. J Comput Phys 2018;363:98–115.
[73] Zhang Y. Critical transition Reynolds number for plane channel flow. Appl Math Mech 2017;38(10):1415–24.
[74] Pereira F, Vaz G, Eça L. An assessment of scale-resolving simulation models for the flow around a circular cylinder. In: Proceedings of the 8th International Symposium on Turbulence, Heat and Mass Transfer (THMT15); 2015.